Monthly Notices of the ROYAL ASTRONOMICAL SOCIETY

MNRAS **489,** 1379–1396 (2019) doi:10.1093/mnras/stz2104
Advance Access publication 2019 August 2

Uncertainties in νp-process nucleosynthesis from Monte Carlo variation of reaction rates

N. Nishimura (西村信哉) [1,2]★† T. Rauscher [3,4]† R. Hirschi,[2,5]† G. Cescutti [4,6]† A. St. J. Murphy[7]† and C. Fröhlich [8]

[1]*Center for Gravitational Physics, Yukawa Institute for Theoretical Physics, Kyoto University, Kyoto 606-8502, Japan*
[2]*Astrophysics Group, Faculty of Natural Sciences, Keele University, Keele ST5 5BG, UK*
[3]*Department of Physics, University of Basel, CH-4056 Basel, Switzerland*
[4]*Centre for Astrophysics Research, University of Hertfordshire, Hatfield AL10 9AB, UK*
[5]*Kavli IPMU (WPI), University of Tokyo, Kashiwa 277-8583, Japan*
[6]*INAF, Osservatorio Astronomico di Trieste, I-34131 Trieste, Italy*
[7]*School of Physics and Astronomy, University of Edinburgh, Edinburgh EH9 3FD, UK*
[8]*Department of Physics, North Carolina State University, Raleigh, NC 27695-8202, USA*

Accepted 2019 July 29. Received 2019 July 29; in original form 2019 March 17

ABSTRACT

It has been suggested that a νp-process can occur when hot, dense, and proton-rich matter is expanding within a strong flux of antineutrinos. In such an environment, proton-rich nuclides can be produced in sequences of proton captures and (n, p) reactions, where the free neutrons are created *in situ* by $\overline{\nu}_e + p \rightarrow n + e^+$ reactions. The detailed hydrodynamic evolution determines where the nucleosynthesis path turns off from $N = Z$ line and how far up the nuclear chart it runs. In this work, the uncertainties on the final isotopic abundances stemming from uncertainties in the nuclear reaction rates were investigated in a large-scale Monte Carlo approach, simultaneously varying more than 10 000 reactions. A large range of model conditions was investigated because a definitive astrophysical site for the νp-process has not yet been identified. The present parameter study provides, for each model, identification of the key nuclear reactions dominating the uncertainty for a given nuclide abundance. As all rates appearing in the νp-process involve unstable nuclei, and thus only theoretical rates are available, the final abundance uncertainties are larger than those for nucleosynthesis processes closer to stability. Nevertheless, most uncertainties remain below a factor of 3 in trajectories with robust nucleosynthesis. More extreme conditions allow production of heavier nuclides but show larger uncertainties because of the accumulation of the uncertainties in many rates and because the termination of nucleosynthesis is not at equilibrium conditions. It is also found that the solar ratio of the abundances of ^{92}Mo and ^{94}Mo could be reproduced within uncertainties.

Key words: neutrino – nuclear reactions, nucleosynthesis, abundances – stars: neutron – stars: abundances – supernovae: general.

1 INTRODUCTION

The νp-process has been proposed to occur when hot, dense, and proton-rich matter is ejected from an astrophysical site under the influence of a strong neutrino flux. Such ejection can be found in the dynamical ejecta of core-collapse supernovae (ccSNe) (Fröhlich et al. 2006a,b), in neutrino-driven proto-neutron-star (PNS) winds (Pruet et al. 2006; Wanajo 2006; Wanajo, Janka & Kubono 2011), in outflows from the massive PNS in 'hypernovae' (Fujibayashi, Yoshida & Sekiguchi 2015), and in outflows from collapsar models (Kizivat et al. 2010). Which sites actually experience a νp-process still partially remains an open question, and the answer to which depends on the detailed hydrodynamic modelling of the outflows and the neutrino emission.

Regardless of the astrophysical site, the general features of the νp-process mainly depend on nuclear properties, such as reaction Q-values and reaction rates. They are briefly described below and in

★ E-mail: nobuya.nishimura@yukawa.kyoto-u.ac.jp
† UK Network for Bridging Disciplines of Galactic Chemical Evolution (BRIDGCE), https://www.bridgce.ac.uk

more detail in Section 3. In a νp-process, starting at ^{56}Ni, sequences of proton captures and (n, p) reactions produce nuclei with larger and larger charge numbers Z and mass numbers A (Fröhlich et al. 2006a,b; Pruet et al. 2006; Wanajo 2006). During most of the nucleosynthesis time-scale, proton captures and (γ, p) reactions are in equilibrium, similarly to an rp-process, and the nucleosynthesis path up to Mo follows the $N = Z$ line in the nuclear chart (see Section 3 for further discussion of the location of the νp-process path). Below 1.5 GK, however, charged particle reactions freeze out quickly, leaving only (n, p) and (n, γ) reactions acting at late time, which push the matter back to stability. After all other reactions have ceased, all remaining unstable nuclides decay to stability through electron captures or β^+ decays.

The amount of nuclei produced in the νp-process is small compared to that in the s- or r-process. Nevertheless, the νp-process may contribute to abundances not dominated by the s- and r-processes. This may be of relevance to explain high abundance ratios of Sr, Y, and Zr relative to Ba in metal-poor stars (François et al. 2007; Montes et al. 2007; Arcones & Bliss 2014). The νp-process could also provide an important contribution to the lighter p-nuclides[1] ^{92,94}Mo and ^{96,98}Ru, which are underproduced in other nucleosynthesis processes such as the γ-process in ccSN (Wanajo et al. 2011; Rauscher et al. 2013; Bliss, Arcones & Qian 2018b).

Any conclusions on the importance of the νp-process depend not only on the choice of site but also on the amount of nuclides and the abundance pattern that can be produced in those sites. Therefore, it is of great interest to study the uncertainties involved in the prediction of the resulting abundances, and especially which possible variation in the production is permitted by the uncertainties in the nuclear reaction rates used. On the one hand, this allows the model uncertainties to be disentangled from the nuclear physics uncertainties, while on the other hand, it provides information on which isotope ratios are permitted because these depend on nuclear properties.

We have developed a Monte Carlo (MC) method allowing the variation of more than 10 000 rates simultaneously to address such questions (Rauscher et al. 2016). A simultaneous variation of rates is necessary to account for the combined action of rate changes. Neglection of such combinations may lead to an overemphasis of certain reactions and a misrepresentation of their impact on the total uncertainty (Rauscher et al. 2016, 2018). The method has been previously applied to investigate nucleosynthesis of p-nuclides in massive stars (Rauscher et al. 2016) and thermonuclear supernovae (Nishimura et al. 2018) and to study the weak s-process in massive stars (Nishimura et al. 2017) and the main s-process in AGB stars (Cescutti et al. 2018). Here, we consistently extend our investigations to quantify the nuclear physics uncertainties in the synthesis of nuclides in the νp-process, applying a similar strategy and input as in the previous studies and allowing a direct comparison of the resulting abundance uncertainties. Due to the fact that there is no single preferred site for the νp-process, a parametrization of astrophysical conditions is used to cover a large range of possibilities.

The contents of this paper are organized as follows: The parametrization of the trajectories used in the MC approach is discussed in Section 2.1. The MC method itself is briefly presented in Section 2.2. The special importance of the 3α reaction and the ^{56}Ni(n, p)^{56}Co reaction in the νp-process is discussed in Section 3.2. The results are shown and discussed in Section 4, and a summary is given in Section 5.

[1]Proton-rich nuclides above Fe, not reached by the s- and r-processes, are called p-nuclides.

2 METHODS

2.1 Astrophysical models

The efficiency of νp-process nucleosynthesis depends on the detailed conditions encountered in the neutrino wind. Among the crucial parameters are initial composition, matter density, and temperature of the ejecta, as well as their expansion rate (determining the time evolution of matter density and temperature) and neutrino wind properties. Since these conditions, on the one hand, are not constrained well by current ccSN explosion models (Bliss et al. 2018a) and, on the other hand, a range of conditions is expected to occur either within one site or in different sites, we investigated a large range of possible environments.

Similar to the ratio of neutron abundance to seed abundance in the r-process, the number ratio Δ_n of free neutrons, created by the reaction p($\overline{\nu}_e$, e$^+$)n, and seed nuclei is a good indicator for the strength of the νp-process, as introduced by Pruet et al. (2006). It is given by

$$\Delta_n \equiv \frac{Y_p}{Y_h} n_{\bar{\nu}_e} = \frac{Y_p}{Y_h} \int_{T_9 \leq 3} \lambda_{\bar{\nu}_e} dt, \quad (1)$$

where $\lambda_{\bar{\nu}_e}$ is the rate for $p + \nu_e \rightarrow n + {}^+e$ and Y_h is the seed abundance, i.e. the abundance of nuclei with $Z > 2$, taken at the onset of the νp-process at $T_9 = 3$. The seed abundance is in large part determined by the abundance of ^{56}Ni. A detailed discussion of the significance of Δ_n is found in Wanajo et al. (2011).

We used a set of parametrized models covering electron fractions of $0.55 \leq Y_e \leq 0.725$ and entropies of $11.4 \leq S \leq 184\ k_B$ baryon^{-1}, taken as initial values at the time of freeze-out from the nuclear statistical equilibrium (NSE) at 7 GK. The choice of Y_e and entropy also determines Δ_n. As illustrated in Fig. 1, within these ranges we probe an extensive set of Δ_n values allowing for a νp-process, from the most feeble onset to strong processing of heavier nuclei. The evolution of temperature and density is based on a typical PNS wind trajectory from a one-dimensional neutrino radiation-hydrodynamic simulation (see, Nishimura et al. 2012, and references therein). Adopting the temperature evolution of the original trajectory, we adjusted the density by multiplying it with a factor consistent with a given entropy.

Examples of the obtained density and temperature as function of time for a few selected trajectories are shown in Fig. 2. In the nucleosynthesis calculations, we only took into account neutrino absorption on nucleons, which is mainly $\bar{\nu}_e + p \rightarrow n + e^+$. The neutrino properties are consistent with the hydrodynamic evolution of a PNS: The values of the luminosity and the mean energy for the anti-electron neutrino are $L_{\bar{\nu}_e} = 2.06 \times 10^{51}$ erg and $\epsilon_{\bar{\nu}_e} =$ 15.2 MeV, respectively, at the beginning of the nucleosynthesis calculations (at 7 GK). The Y_e did not change significantly (only decreased by ∼0.005) between the end of NSE and the end of the νp-process nucleosynthesis. The details of the trajectories used in the MC study are also summarized in Table 1.

2.2 Nucleosynthesis with MC variations

The trajectories (see Section 2.1) were post-processed using the PIZBUIN code suite, consisting of a fast reaction network and a parallelized MC driver. Our reaction network calculations started at

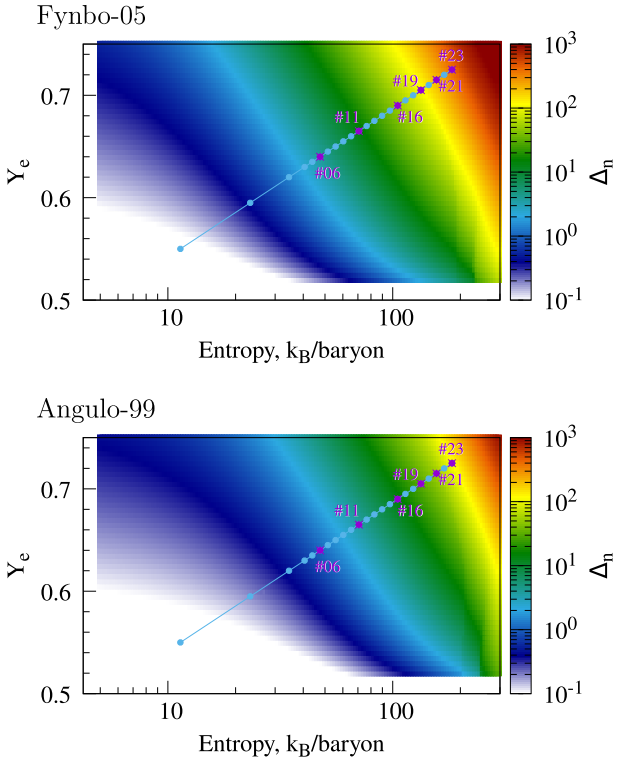

Figure 1. The explored parameter space in Y_e and entropy S for two choices of the 3α reaction rate. Dots correspond to trajectories used for the MC variations.

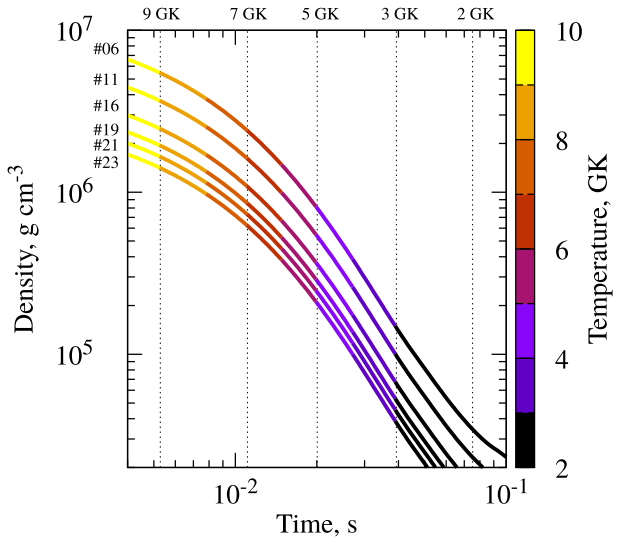

Figure 2. Time evolution (after the core bounce) of matter density for selected trajectories, based on the neutrino-driven wind component from PNS surface (Nishimura et al. 2012). The colour of each line shows the temperature at a given time.

$T = 7$ GK and followed the nucleosynthesis throughout the freeze-out and final decay back to stability. We used the same procedure as presented in detail in Rauscher et al. (2016) and previously applied to various further nucleosynthesis sites (see Section 1). Therefore, only the main points of the procedure are briefly summarized here.

The reaction network contained 2216 nuclides, including nuclides around stability and towards the proton-rich side of the

Table 1. Initial conditions for each explored trajectory; the shown values of Δ_n were obtained using the 3α reaction rate by Fynbo et al. (2005) (Fynbo-05) and by Angulo et al. (1999) (Angulo-99), respectively. The six trajectories labelled in Fig. 1 are underlined.

Trajectory	Y_e	Entropy (k_B baryon^{-1})	Δ_n Fynbo-05	Δ_n Angulo-99
#01	0.550	11.4	6.15×10^{-2}	4.57×10^{-2}
#02	0.595	23.2	0.356	0.158
#03	0.620	34.6	1.15	0.372
#04	0.630	40.5	1.89	0.561
#05	0.635	43.9	2.43	0.698
#06	0.640	47.5	3.13	0.873
#07	0.645	51.5	4.05	1.10
#08	0.650	55.7	5.22	1.40
#09	0.655	60.3	6.77	1.79
#10	0.660	65.3	8.74	2.30
#11	0.665	70.7	11.3	2.97
#12	0.670	76.6	14.7	3.85
#13	0.675	82.9	19.0	4.99
#14	0.680	89.7	24.7	6.50
#15	0.685	97.2	32.0	8.50
#16	0.690	105	41.4	11.1
#17	0.695	114	53.7	14.6
#18	0.700	123	69.4	19.1
#19	0.705	134	89.6	24.9
#20	0.710	145	1.17×10^2	32.6
#21	0.715	157	1.63×10^2	42.6
#22	0.720	169	2.23×10^2	58.0
#23	0.725	184	3.05×10^2	84.7

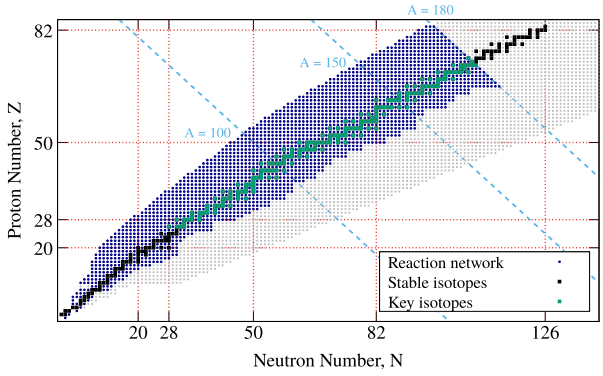

Figure 3. Nuclides included in the reaction network on the N–Z plane.

nuclear chart, as shown in Fig. 3. The standard rate set and the assigned uncertainties were the same as previously used in our works (Rauscher et al. 2016; Nishimura et al. 2017, 2018; Cescutti et al. 2018): rates for neutron-, proton-, and α-induced reactions were a combination of theoretical values given by Rauscher & Thielemann (2000) and supplemented by experimental rates taken from Dillmann et al. (2006) and Cyburt et al. (2010). Decays and electron captures were taken from a REACLIB file compiled by Freiburghaus & Rauscher (1999) and supplemented by rates from Takahashi & Yokoi (1987) and Goriely (1999) as provided by Aikawa et al. (2005) and Xu et al. (2013).

Each trajectory was run 10 000 times in a network calculation, with each rate subject to a different rate variation factor for each run. The combined output was then analysed. For each trajectory, the total uncertainty in the final abundances after decay to stability was calculated and key rates, i.e. those that dominate the uncertainty of a given final isotopic abundance, were identified. By our definition,

reducing the uncertainty of a key rate will also considerably decrease the uncertainty in a final abundance. The identification of key rates was achieved by examining the correlation between a change in a rate and the change of an abundance, as found in the stored MC data. As before, the Pearson product–moment correlation coefficient (Pearson & Galton 1895) was used to quantify correlations. Pearson correlation coefficient $r_{\rm cor}$ can assume values $0 \leq |r| \leq 1$. Positive values of $r_{\rm cor}$ indicate a direct correlation between rate change and abundance change, whereas negative values signify an inverse correlation, i.e. the abundance decreases when the rate is increased. The larger the absolute value of the Pearson coefficient, the stronger the correlation. As in our previous work, a key rate was identified by $|r_{\rm cor}| \geq 0.65$.

Each astrophysical reaction rate on target nuclides from light nuclei to Bi was varied within its own uncertainty range. Forward and reverse rates received the same variation factor, as they are connected by detailed balance. The assigned uncertainty range is temperature dependent and constructed from a combination of the measured uncertainty (if available) for target nuclei in their ground states and a theory uncertainty for predicted rates on nuclei in thermally excited states. Theory uncertainties were different depending on the reaction type and can be asymmetric. Details are given in Rauscher et al. (2016, 2018). In the present context, it is important to note that the nucleosynthesis path is located a few units away from stability and therefore there are no experimentally determined reaction rates available (except for the 3α reaction and a few reactions acting on stable nuclides at late times; see Section 4). Furthermore, the temperatures in the νp-process are so high that reactions on thermally excited states of nuclei dominate the reaction rate (Rauscher 2012, 2014) and these are not constrained experimentally. Thus, effectively the uncertainties in the reaction rates were dominated by the assumed theory uncertainties. For example, the two most important reaction types, (n,p)↔(p,n) and (p,γ)↔(γ,p), were varied from 1/3 the standard rate to twice the standard rate and (p,α)↔(α,p) rates were varied between 1/10 and twice the standard rate.

The present MC study does not include uncertainties on nuclear masses. Nevertheless, it is worth noting that uncertainties in the nuclear masses affect the equilibrium abundances within an isotonic chain established by the $(\mathrm{p},\gamma)-(\gamma,\mathrm{p})$ equilibrium (see Sections 1 and 3.1) because they change the ratio of forward and reverse reactions. Compared to the situation in the rp-process, however, uncertainties in mass differences, which affect the proton separation energies, are of lesser importance in the νp-process. This is due to the different hydrodynamic conditions, the dominance of fast (n, p) reactions over competing proton captures or β^+ decays, and the different location of the νp-process path, proceeding closer to stability and involving fewer nuclides with inaccurately determined masses. Wanajo et al. (2011) quote a number of nuclides for which nuclear masses should be determined with smaller uncertainty. A number of experimental investigations have targeted masses of nuclides in the νp-process path (see, e.g. Weber et al. 2008; Haettner et al. 2011; Xing et al. 2018).

3 THE FEATURES OF νP-PROCESS NUCLEOSYNTHESIS

3.1 General

A νp-process can occur in proton-rich hot ejecta expanding in a flow of anti-electron neutrinos ($\overline{\nu}_{\rm e}$). The ejecta quickly cool from the initially very high temperature, at which time only nucleons were present. In the first phase of the cooling, nucleons are assembled mainly to ^{56}Ni and α-particles in an NSE, leaving a large number of free protons. At sufficiently low temperature (≤3–4 GK), rapid proton captures ensue on ^{56}Ni. Production of heavier nuclei would be stopped at ^{64}Ge, which has an electron-capture lifetime longer than a minute. This is too long in comparison with the expansion time-scale (of the order of seconds) to allow for production of an appreciable number of nuclides beyond ^{64}Ge before nuclear reactions freeze out. In the νp-process, however, a small number of free neutrons are continuously created by $\overline{\nu}_{\rm e}$ captures on the free protons. This supply of free neutrons allows for (n, p) reactions bypassing any slow electron captures and β^+ decays, not just of ^{64}Ge but also of other potential bottlenecks at a higher mass number.

The main nucleosynthesis flow in the νp-process is characterized by rapid proton captures in a (p,γ)–(γ,p) equilibrium, with (n, p) reactions connecting the contiguous isotonic chains. Although such an equilibrium is also achieved in the rp-process on the surface of accreting neutron stars (Schatz et al. 1998), the νp-process proceeds at lower density than the rp-process. The resulting nucleosynthesis path follows the $N = Z$ line only up to the Mo region, reaching further and further into neutron-richer isotopes between Mo and Sn, moving gradually away from the $N = Z$ line (Wanajo et al. 2011). The path is pushed strongly towards stability at the Sn isotopes and above, providing a strong barrier for the efficient production of any elements beyond Sn. Decay and (n, p) reaction time-scales are longer for nuclides closer to stability, and the higher Coulomb barriers suppress proton captures.

The location of the effective νp-process path is determined by the nuclear properties, giving rise to the (p,γ)–(γ,p) equilibrium and the very fast (n, p) reactions, and remains remarkably unaffected by variations of the astrophysical parameters within realistic limits such as entropy, $Y_{\rm e}$, and expansion time-scale, as long as the conditions permit the appearance of a νp-process. Whenever a νp-process occurs, the nucleosynthesis path beyond ^{56}Ni initially follows the $N = Z$ line and gradually veers off towards stability. Systematic variations of reaction rates show only small effects, if any, regarding the path location. This is a consequence of the (p,γ)–(γ,p) equilibrium in which the path is determined by nuclear mass differences (Schatz et al. 1998). All these variations, however, determine how far up the path follows the $N = Z$ line before diverging, or whether it is terminated already at low charge numbers, Z. Consequently, it is clear that the achieved abundances within the path are also determined by these conditions. This motivates the introduction of quantity $\Delta_{\rm n}$ as defined in equation (1).

On the nuclear reaction side, it is expected that the results are mostly insensitive to proton captures due to the prevailing (p,γ)–(γ,p) equilibrium. Only at late freeze-out times does this equilibrium break down, giving rise to some sensitivity to a variation of rates. There may also be some sensitivity to proton captures located at the end of the nucleosynthesis path that are not, or only barely, in equilibrium.

The flow to heavier nuclei is determined by (n, p) reactions and thus a knowledge of these is essential. For a given choice of astrophysical conditions, faster (n, p) rates result in processing further up the nucleosynthesis path. Whether a given (n, p) reaction is important, however, depends on whether its target nucleus is actually in the path and whether it receives an appreciable abundance as given by the (p,γ)–(γ,p) equilibrium. Neutron captures on proton-rich nuclei may be of some relevance at large Z and/or at late times, depending on the hydrodynamic evolution of the trajectory (Wanajo et al. 2011; Arcones, Fröhlich & Martínez-Pinedo 2012).

A special class of reactions are those that govern the onset of the νp-process at high temperature. When freezing out from NSE at high temperature, the νp-process is delayed by several factors. At high temperature, (γ, p) reactions are fast and the equilibrium abundances are always located around ^{56}Ni. Since the main abundance is concentrated in ^{56}Ni, further processing is halted until the ^{56}Ni waiting point can be bridged effectively and the (p, γ)–(γ, p) equilibrium abundance maxima in the subsequent isotonic chains are moved to higher Z. This depends on the competing rates of (γ, p), (n, γ), and (n, p) on ^{56}Ni and occurs at $T \approx 3.5$ GK.

Whether further processing occurs at this temperature depends on the relative speeds of (γ, α), (p, α), and (n, α) reactions on waiting point isotopes of Zn and Ge compared to the (n, p), (n, γ), or (p, γ) reactions required to commence the nucleosynthesis to heavier elements. It has been shown that reaction cycles can form via (n, α) or (p, α) reactions and further delay the processing to heavier mass (Arcones et al. 2012; Rauscher 2014). Since these depend on competitions between particle-induced reactions, they do not depend strongly on the time dependence of the density imposed by a chosen trajectory. A modification of the density at a given temperature affects proton- and neutron-induced reactions similarly and only changes the relation between proton captures and (γ, p) reactions. The strongest dependence on an astrophysical parameter is the one on Y_n created by the $\overline{\nu}_e$ flux present at a given temperature. However, this does not change the ratio between (n, γ), (n, p), and (n, α) reactions, the latter being a hindrance to the flow up to heavier nuclei. Another important aspect is the time evolution of the trajectory because it determines for how long favourable conditions for a cycle (if existing) are upheld.

In our MC variation study, we do not explicitly inspect reaction flows but, of course, the above cases are accounted for in the network runs automatically and thus are implicitly included in the analysis of final abundances and key reactions given in Section 4.

3.2 Importance of the 'bottleneck' reactions: 3α and ^{56}Ni(n, p)^{56}Co

While the MC variations focus on the production of Fe isotopes and above, it is important to note that the efficiency of νp-process nucleosynthesis strongly depends on the 3α reaction (the two-step reaction with the first step being $^4\mathrm{He} + {}^4\mathrm{He} \rightarrow {}^8\mathrm{Be}$, immediately followed by $^8\mathrm{Be} + {}^4\mathrm{He} \rightarrow {}^{12}\mathrm{C}$), which thus is an important key reaction. It is never in equilibrium and determines the relative abundance of α-particles, protons, and ^{56}Ni at the onset and during the νp-process. It therefore determines the ^{56}Ni seed available for further processing up to heavier masses and thus also plays a dominant role in the production of heavy nuclei. Despite the importance of this reaction, the 3α reaction bears a large experimental uncertainty in the high temperature regime as well as in the lower temperature region, the latter being mainly important for stellar evolution.

Fig. 4 presents the 3α reaction rates, together with their uncertainties, as determined by Fynbo et al. (2005) (as given in the JINA REACLIB) and Angulo et al. (1999) (as given in Sallaska et al. 2013). The older rate of Caughlan & Fowler (1988) (also given in the JINA REACLIB) is also shown. In Fig. 5, we show the final MC-computed abundances, and their uncertainties, obtained with the 3α reaction rate of Fynbo et al. (2005) and its uncertainty as given in Fig. 5, for the trajectories #06, #11, #16, #19, #21, and #23 (see Table 1). The impact of the 3α reaction rate on the production of nuclides in all trajectories is summarized in Fig. 6. As is obvious from Fig. 5, the variation in final abundances is so

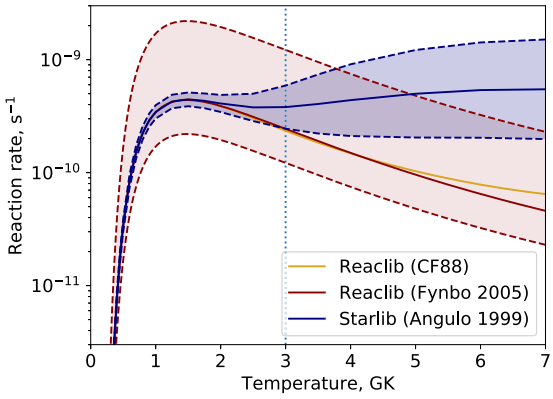

Figure 4. Comparison of 3α reaction rates as a function of temperature. The uncertainty factor assigned to the rate of Fynbo et al. (2005) was ×5 upwards and ×0.5 downwards. The reaction rate by Angulo et al. (1999) was adopted with the `Starlib` uncertainty evaluation. The older standard rate by Caughlan & Fowler (1988) (CF88) is also plotted. It is close to the Fynbo et al. (2005) rate at low temperature.

strong that it would cover most variations caused by uncertainties in rates involving nuclides heavier than Fe. Therefore, we chose a 'standard' rate for the 3α reaction and did not vary it further during the MC procedure. Our 'standard' rate is the one of Fynbo et al. (2005) as given in the JINA REACLIB.

Fig. 1 and Table 1 provide Δ_n values for the two choices of 3α reaction rates. As can be seen easily in Table 1, the choice of 3α reaction rate affects at which initial conditions a specific value of Δ_n is achieved. For example, using the Fynbo et al. (2005) rate, a value of $\Delta_n \approx 19$ is found in trajectory #13 whereas a similar value is found in trajectory #18 for the Angulo et al. (1999) rate. This explains why the overall production patterns are shifted in Fig. 8 when comparing the results obtained with these two rates. Trajectories with larger Δ_n produce heavier nuclei because with a larger supply of neutrons the nucleosynthesis path can run further up to larger mass numbers. A slower 3α reaction rate leaves more protons at the onset of the processing and thus reduces the ^{56}Ni seed.

Wanajo et al. (2011) identified two reaction sequences competing with the 3α reaction. These sequences are determined by the reactions $^7\mathrm{Be}(\alpha, \gamma)^{11}\mathrm{C}$ and $^{10}\mathrm{B}(\alpha, p)^{13}\mathrm{C}$. Their uncertainties have a similar impact as the one in the 3α reaction discussed above.

Another crucial reaction is ^{56}Ni(n, p)^{56}Co. It is the first reaction in the path converting the ^{56}Ni seed to heavier nuclides. Therefore, it determines the efficiency of the νp-process and all abundances created, regardless of the detailed conditions. Fig. 7 shows the impact of a variation of the ^{56}Ni(n, p)^{56}Co reaction rate on abundances in all trajectories. Similar to the 3α reaction rate, the resulting abundances are extremely sensitive to this rate. Therefore, we do not include this reaction in the further MC rate variations as its uncertainty would cover all other uncertainties. The results presented in Section 4 were obtained using the ^{56}Ni(n, p)^{56}Co rate of Rauscher & Thielemann (2000).

4 RESULTS AND DISCUSSION

Based on the thermodynamical parameters described in Section 2.1 and given in Table 1, we performed nucleosynthesis calculations with the nuclear reaction network specified in Section 2.2. The final mass fractions of nuclei produced in the νp-process for selected

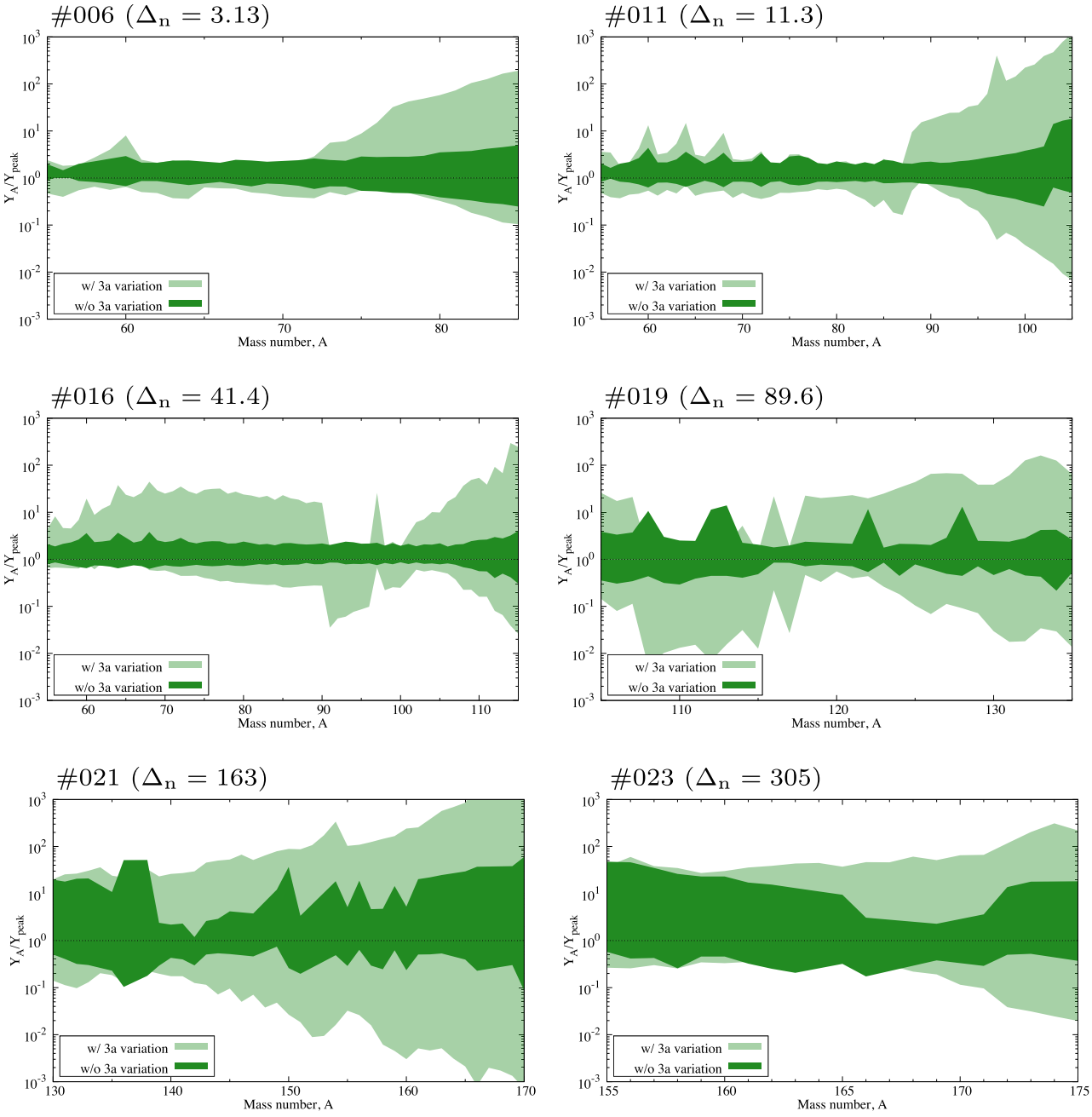

Figure 5. Final uncertainties obtained in six selected trajectories with and without variations of the 3α reaction rate. The colour shade corresponds to a 90 per cent probability interval for each isobaric abundance (Y_A), normalized to the peak value (Y_{peak}).

trajectories are shown in Fig. 8. For comparison, in Fig. 8 the obtained mass fractions are shown for two 3α reaction rates found in literature (as discussed in Section 3.2).

For trajectories #06, #11, #16, #19, #21, and #23, the total uncertainties originating from the combined action of all varied rates are given in Tables 2 and 3 and shown in Figs 9 and 10, respectively. Only nuclides that are produced with mass fractions larger than 2×10^{-5} are included in these figures and tables. The 'up' and 'down' factors in Tables 2 and 3 are to be taken relative to the abundance value Y_{50} (50 per cent of the cumulative frequency for the Y distribution). They encompass the range of abundance values obtained in 90 per cent of the MC runs and can be viewed as a 90 per cent confidence interval. The abundance Y_{peak}, on the other hand, is the abundance value at the peak of the probability distribution, i.e. the most probable abundance when considering all MC variations. The values of Y_{50} and Y_{peak} do not have to coincide because the probability distribution is asymmetric. Especially for very flat distributions, Y_{50} may differ considerably from Y_{peak}. The probability distribution is visualized by the colour shade for each nuclide in Figs 9 and 10. For further details, see fig. 5 in Rauscher et al. (2016) and fig. 2 in Nishimura et al. (2017) and the detailed discussion in section 2.3 of Rauscher et al. (2016).

We find generally larger production uncertainties than those in our previous studies of other nucleosynthesis processes but still mostly below a factor of 3 for the trajectories below #19. The uncertainties become larger in trajectory #19 and above, eventually

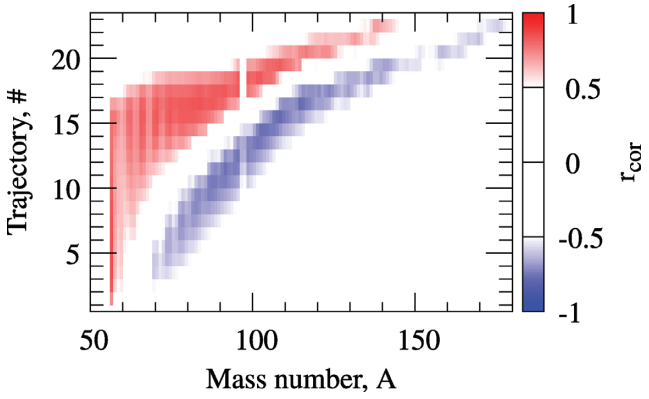

Figure 6. The impact of the 3α reaction rate (Fynbo et al. 2005) on the production of nuclides for all trajectories. Shown is the correlation of the abundance variation of a given nuclide with the variation of the 3α reaction rate.

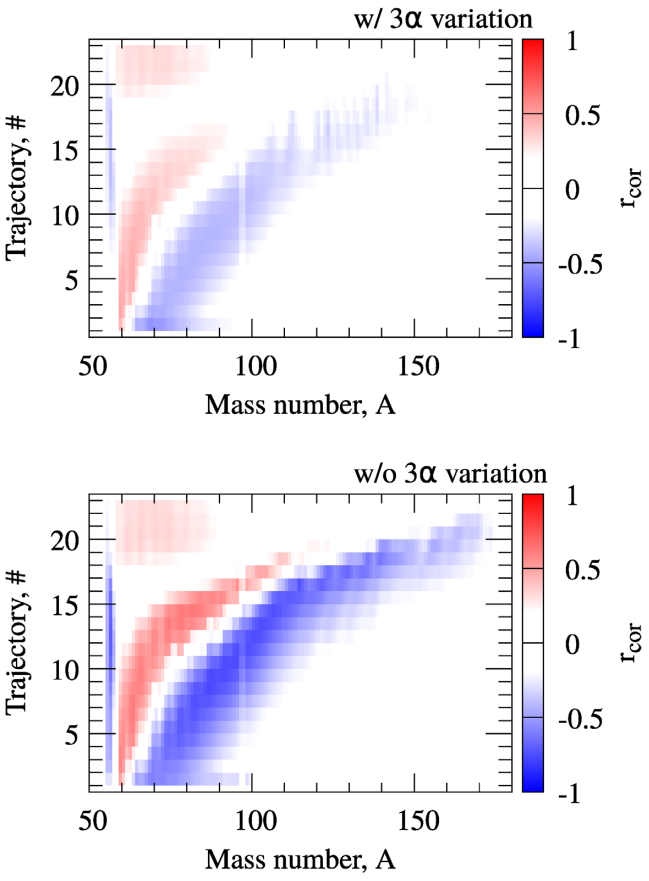

Figure 7. The impact of the ^{56}Ni(n, p)^{56}Co rate on the production of nuclides for all trajectories. Shown is the correlation of the abundance variation of a given nuclide with the variation of the ^{56}Ni(n, p)^{56}Co reaction rate, with (top panel) and without (bottom panel) simultaneous variation of the 3α reaction rate.

reaching factors of about 40 in trajectories #21 and #23. The reason for this increase is that these trajectories mainly produce the heavier mass range and the efficiency of the flow towards heavier nuclides is impacted by all the reactions starting from ^{56}Ni. Whether or not the heavier nuclides can be produced at all and where the nucleosynthesis path lies are determined by the common action of all

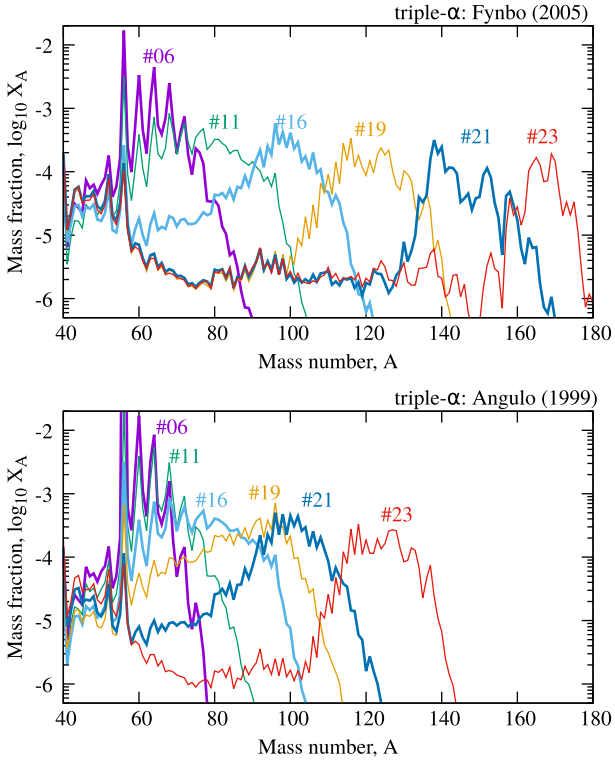

Figure 8. Final mass fractions obtained in selected trajectories and with two different 3α reaction rates. All other rates have not been varied but kept at their standard values.

reactions in the path. Furthermore, the far end of the nucleosynthesis path is not reached in equilibrium, making individual reactions, and competition between them, more important. In consequence, many reaction uncertainties are convolved, the combined effect strongly 'wagging the tail' of the path in the heavier mass range. This is also reflected in the fact that no key rates (see below) were found in trajectories #19–#23.

Key rates are those rates that dominate the uncertainty of a given nuclide. Key rates identified in all the investigated trajectories are given in Tables 4–6. It should be noted that only rates for target nuclides of Fe and above were varied and the 3α reaction rate and the ^{56}Ni(n, p)^{56}Co rate were kept at their chosen standard descriptions for these cases (see Section 3.2). For which nuclides key rates appear for a given trajectory mainly depends on how far up to larger mass numbers the reaction flow continues. On the other hand, as can be seen in Fig. 8, trajectories producing heavier nuclides underproduce the lighter mass range. This trend is reflected in the key rate tables, which do not show key rates for lighter nuclides for trajectories producing the heavier mass range. Furthermore, even when nuclides are produced at an appreciable level, not all of them have their uncertainty connected to a single key rate. In this case, several rates contribute to the production uncertainty, with none of them dominating the contribution to the total uncertainty.

As in our previous investigations, key rates were assigned different levels. The most important rates are at level 1. Level 2 key rates are found after removing the level 1 rates from the MC variations. They determine the uncertainty in the production of a given nuclide assuming that the level 1 key rate has been determined. Similarly, level 3 key rates are defined as dominating the abundance

Table 2. Total production uncertainties for stable nuclides after decay of progenitors made in the νp-process. The abundance $Y_{\rm peak}$ is the peak value of the final abundance probability distribution from our MC runs. The uncertainty factors shown for variations up and down enclose a 90 per cent probability interval and are relative to Y_{50} (trajectories #06, #11, and #16).

	(#06)				(#11)				(#16)			
Nuclide	Up	Down	Y_{50}	$Y_{\rm peak}$	Up	Down	Y_{50}	$Y_{\rm peak}$	Up	Down	Y_{50}	$Y_{\rm peak}$
^{58}Ni	2.07	0.750	1.38×10^{-6}	1.64×10^{-6}	2.00	0.734	5.13×10^{-7}	6.08×10^{-7}				
^{60}Ni	3.04	0.694	3.71×10^{-5}	4.98×10^{-5}	5.23	0.753	3.58×10^{-6}	5.55×10^{-6}	3.73	0.671	2.15×10^{-7}	2.89×10^{-7}
^{61}Ni	1.74	0.707	6.36×10^{-6}	6.75×10^{-6}	1.96	0.727	1.52×10^{-6}	1.80×10^{-6}				
^{62}Ni	1.72	0.704	2.68×10^{-6}	2.85×10^{-6}	1.76	0.657	8.55×10^{-7}	9.08×10^{-7}				
^{63}Cu	2.14	0.713	1.47×10^{-5}	1.74×10^{-5}	2.28	0.685	2.82×10^{-6}	3.35×10^{-6}				
^{64}Zn	2.45	0.734	4.69×10^{-5}	6.31×10^{-5}	3.75	0.672	7.23×10^{-6}	9.72×10^{-6}	3.80	0.666	2.50×10^{-7}	3.36×10^{-7}
^{66}Zn	1.73	0.674	5.02×10^{-6}	5.33×10^{-6}	1.84	0.798	1.90×10^{-6}	2.26×10^{-6}				
^{67}Zn	2.22	0.670	7.65×10^{-6}	9.08×10^{-6}	2.21	0.720	2.57×10^{-6}	3.05×10^{-6}				
^{68}Zn	2.15	0.608	2.81×10^{-5}	3.34×10^{-5}	4.12	0.764	6.57×10^{-6}	1.02×10^{-5}	3.94	0.649	2.13×10^{-7}	2.86×10^{-7}
^{69}Ga	2.03	0.696	6.47×10^{-6}	7.68×10^{-6}	1.79	0.682	4.89×10^{-6}	5.19×10^{-6}				
^{71}Ga	1.96	0.560	5.16×10^{-6}	5.48×10^{-6}	2.08	0.736	3.59×10^{-6}	4.26×10^{-6}				
^{70}Ge	1.88	0.604	2.44×10^{-6}	2.59×10^{-6}	1.81	0.687	2.26×10^{-6}	2.40×10^{-6}				
^{72}Ge	2.38	0.535	8.25×10^{-6}	9.79×10^{-6}	3.48	0.670	5.13×10^{-6}	6.90×10^{-6}	2.96	0.721	1.95×10^{-7}	2.62×10^{-7}
^{73}Ge	1.97	0.544	2.27×10^{-6}	2.41×10^{-6}	1.76	0.671	3.28×10^{-6}	3.49×10^{-6}				
^{75}As	2.97	0.554	2.23×10^{-6}	3.00×10^{-6}	2.63	0.667	3.39×10^{-6}	4.03×10^{-6}				
^{74}Se	1.91	0.538	1.13×10^{-6}	1.20×10^{-6}	1.70	0.700	2.20×10^{-6}	2.34×10^{-6}				
^{76}Se	2.89	0.541	1.94×10^{-6}	2.61×10^{-6}	3.10	0.722	3.56×10^{-6}	4.79×10^{-6}	2.21	0.652	2.12×10^{-7}	2.52×10^{-7}
^{77}Se	2.93	0.502	1.32×10^{-6}	1.78×10^{-6}	2.47	0.671	4.61×10^{-6}	5.48×10^{-6}	1.97	0.594	2.88×10^{-7}	3.06×10^{-7}
^{79}Br	3.08	0.464	3.34×10^{-7}	4.49×10^{-7}	1.62	0.689	2.86×10^{-6}	3.04×10^{-6}	1.79	0.593	2.50×10^{-7}	2.65×10^{-7}
^{78}Kr	2.59	0.435	3.85×10^{-7}	4.57×10^{-7}	1.70	0.682	2.40×10^{-6}	2.55×10^{-6}	1.98	0.691	2.09×10^{-7}	2.48×10^{-7}
^{80}Kr	3.21	0.356	3.88×10^{-7}	4.61×10^{-7}	2.06	0.748	3.12×10^{-6}	3.70×10^{-6}	2.18	0.658	4.15×10^{-7}	4.92×10^{-7}
^{82}Kr					1.60	0.710	2.95×10^{-6}	3.13×10^{-6}	1.68	0.648	5.31×10^{-7}	5.64×10^{-7}
^{83}Kr					1.77	0.672	2.63×10^{-6}	2.79×10^{-6}	1.73	0.629	4.29×10^{-7}	4.55×10^{-7}
^{85}Rb					2.24	0.707	1.88×10^{-6}	2.24×10^{-6}	1.80	0.614	3.65×10^{-7}	3.87×10^{-7}
^{84}Sr					1.62	0.711	2.01×10^{-6}	2.14×10^{-6}	1.63	0.657	5.98×10^{-7}	6.35×10^{-7}
^{86}Sr					2.13	0.713	1.93×10^{-6}	2.29×10^{-6}	1.82	0.628	5.74×10^{-7}	6.10×10^{-7}
^{87}Sr					1.68	0.656	1.55×10^{-6}	1.64×10^{-6}	1.73	0.634	5.45×10^{-7}	5.79×10^{-7}
^{88}Sr					1.64	0.660	1.41×10^{-6}	1.50×10^{-6}	1.68	0.683	8.52×10^{-7}	9.05×10^{-7}
^{89}Y					1.99	0.695	1.11×10^{-6}	1.32×10^{-6}	1.92	0.717	5.38×10^{-7}	6.39×10^{-7}
^{90}Zr					2.04	0.676	1.28×10^{-6}	1.52×10^{-6}	1.99	0.721	8.36×10^{-7}	9.93×10^{-7}
^{91}Zr					1.92	0.659	1.11×10^{-6}	1.31×10^{-6}	1.65	0.700	1.38×10^{-6}	1.47×10^{-6}
^{92}Nb									2.54	0.491	2.38×10^{-7}	2.83×10^{-7}
^{93}Nb					1.68	0.469	7.74×10^{-7}	7.44×10^{-7}	2.45	0.809	7.94×10^{-7}	1.07×10^{-6}
^{92}Mo					1.76	0.556	1.01×10^{-6}	1.07×10^{-6}	2.11	0.740	1.59×10^{-6}	1.89×10^{-6}
^{94}Mo					2.15	0.550	7.59×10^{-7}	9.01×10^{-7}	2.11	0.730	1.91×10^{-6}	2.27×10^{-6}
^{95}Mo					2.30	0.499	5.14×10^{-7}	6.10×10^{-7}	1.96	0.722	1.43×10^{-6}	1.70×10^{-6}
^{96}Mo									3.12	0.546	1.80×10^{-7}	2.43×10^{-7}
^{97}Tc					3.03	0.435	2.46×10^{-7}	3.30×10^{-7}	2.05	0.690	1.86×10^{-6}	2.21×10^{-6}
^{96}Ru					2.51	0.417	8.55×10^{-7}	1.02×10^{-6}	1.81	0.659	4.54×10^{-6}	4.82×10^{-6}
^{98}Ru					3.78	0.465	1.31×10^{-7}	2.03×10^{-7}	1.60	0.680	3.50×10^{-6}	3.72×10^{-6}
^{99}Ru									1.79	0.641	1.93×10^{-6}	2.05×10^{-6}
^{100}Ru									1.58	0.708	3.56×10^{-6}	3.78×10^{-6}
^{101}Ru									1.94	0.726	1.83×10^{-6}	2.17×10^{-6}
^{103}Rh									1.90	0.731	1.23×10^{-6}	1.46×10^{-6}
^{102}Pd									1.55	0.702	2.42×10^{-6}	2.57×10^{-6}
^{104}Pd									1.68	0.669	1.64×10^{-6}	1.75×10^{-6}
^{105}Pd									2.00	0.714	8.51×10^{-7}	1.01×10^{-6}
^{106}Pd									2.24	0.660	3.32×10^{-7}	3.94×10^{-7}
^{107}Ag									1.69	0.629	8.97×10^{-7}	9.53×10^{-7}
^{109}Ag									2.22	0.578	4.92×10^{-7}	5.84×10^{-7}
^{106}Cd									1.60	0.627	1.53×10^{-6}	1.62×10^{-6}
^{108}Cd									1.73	0.554	1.13×10^{-6}	1.20×10^{-6}
^{110}Cd									2.36	0.511	4.57×10^{-7}	5.42×10^{-7}
^{111}Cd									2.40	0.505	2.67×10^{-7}	3.17×10^{-7}
^{113}In									2.88	0.513	2.49×10^{-7}	3.35×10^{-7}
^{112}Sn									3.07	0.414	3.55×10^{-7}	4.78×10^{-7}
^{114}Sn									3.82	0.497	1.39×10^{-7}	2.16×10^{-7}

Table 3. Total production uncertainties for stable nuclides after decay of progenitors made in the νp-process. The uncertainty factors shown for variations up and down enclose a 90 per cent probability interval (trajectories #19, #21, and #23).

	(#19)				(#21)				(#23)			
Nuclide	Up	Down	Y_{50}	Y_{peak}	Up	Down	Y_{50}	Y_{peak}	Up	Down	Y_{50}	Y_{peak}
^{104}Pd	6.85	0.441	7.69×10^{-8}	1.72×10^{-7}								
^{106}Pd	3.87	0.433	1.25×10^{-7}	1.93×10^{-7}								
^{109}Ag	4.24	0.444	2.04×10^{-7}	3.73×10^{-7}								
^{108}Cd	8.30	0.340	1.35×10^{-7}	3.89×10^{-7}								
^{110}Cd	1.70	0.197	7.59×10^{-7}	6.66×10^{-7}								
^{111}Cd	1.66	0.262	3.77×10^{-7}	3.31×10^{-7}								
^{113}In	10.9	0.345	5.13×10^{-8}	1.48×10^{-7}								
^{112}Sn	12.4	0.484	1.08×10^{-7}	4.34×10^{-7}								
^{114}Sn	1.66	0.300	1.82×10^{-6}	1.75×10^{-6}								
^{115}Sn	1.52	0.357	8.24×10^{-7}	7.92×10^{-7}								
^{116}Sn	1.33	0.631	2.39×10^{-6}	2.30×10^{-6}								
^{117}Sn	1.61	0.689	8.08×10^{-7}	8.58×10^{-7}								
^{118}Sn	2.16	0.649	1.11×10^{-6}	1.32×10^{-6}								
^{119}Sn	2.09	0.703	5.94×10^{-7}	7.05×10^{-7}								
^{121}Sb	1.75	0.584	8.72×10^{-7}	9.26×10^{-7}								
^{123}Sb	1.46	0.708	1.25×10^{-6}	1.32×10^{-6}								
^{122}Te	9.04	0.417	1.10×10^{-7}	3.17×10^{-7}								
^{124}Te	1.58	0.328	1.23×10^{-6}	1.18×10^{-6}								
^{125}Te	1.72	0.638	1.09×10^{-6}	1.16×10^{-6}								
^{126}Te	1.50	0.449	1.69×10^{-6}	1.62×10^{-6}								
^{127}I	3.44	0.588	5.37×10^{-7}	8.33×10^{-7}								
^{129}Xe	2.26	0.647	4.24×10^{-7}	5.03×10^{-7}								
^{130}Xe	1.98	0.379	5.19×10^{-7}	5.52×10^{-7}								
^{131}Xe	2.17	0.567	5.74×10^{-7}	6.81×10^{-7}								
^{132}Xe	2.59	0.407	5.68×10^{-7}	6.75×10^{-7}	37.3	0.577	1.65×10^{-8}	1.10×10^{-7}				
^{133}Cs	5.94	0.604	1.69×10^{-7}	3.10×10^{-7}	37.8	0.546	1.86×10^{-8}	1.24×10^{-7}				
^{135}Ba	2.38	0.476	2.36×10^{-7}	2.81×10^{-7}	19.5	0.414	5.08×10^{-8}	3.40×10^{-7}				
^{136}Ba	2.37	0.352	3.65×10^{-7}	3.87×10^{-7}								
^{139}La	4.61	0.338	8.25×10^{-8}	1.28×10^{-7}	1.96	0.240	1.05×10^{-6}	1.12×10^{-6}				
^{140}Ce					1.62	0.319	1.63×10^{-6}	1.57×10^{-6}				
^{142}Ce					1.52	0.390	5.89×10^{-7}	5.66×10^{-7}				
^{141}Pr					1.71	0.294	5.22×10^{-7}	5.02×10^{-7}				
^{143}Nd					2.71	0.525	4.04×10^{-7}	5.44×10^{-7}				
^{144}Nd					3.00	0.557	3.11×10^{-7}	4.18×10^{-7}				
^{145}Nd					4.33	0.536	1.80×10^{-7}	2.42×10^{-7}				
^{147}Sm					5.34	0.651	1.45×10^{-7}	2.66×10^{-7}				
^{149}Sm					13.1	0.808	3.80×10^{-8}	1.53×10^{-7}				
^{151}Eu					4.02	0.236	2.04×10^{-7}	3.16×10^{-7}				
^{155}Gd					7.25	0.408	5.82×10^{-8}	1.07×10^{-7}				
^{157}Gd					10.3	0.652	6.34×10^{-8}	1.83×10^{-7}				
^{158}Gd					8.19	0.424	1.05×10^{-7}	2.36×10^{-7}	47.2	0.465	1.83×10^{-8}	1.23×10^{-7}
^{159}Tb					8.73	0.376	8.21×10^{-8}	1.84×10^{-7}	41.8	0.826	1.76×10^{-8}	1.18×10^{-7}
^{161}Dy									30.9	0.585	1.68×10^{-8}	1.12×10^{-7}
^{162}Dy									28.0	0.456	2.48×10^{-8}	1.66×10^{-7}
^{163}Dy									23.6	0.374	4.99×10^{-8}	3.34×10^{-7}
^{165}Ho									17.0	0.579	1.18×10^{-7}	7.91×10^{-7}
^{166}Er									4.33	0.245	2.95×10^{-7}	5.40×10^{-7}
^{169}Tm									1.87	0.311	8.42×10^{-7}	8.94×10^{-7}
^{171}Yb									4.31	0.346	2.25×10^{-7}	3.49×10^{-7}
^{172}Yb									14.9	0.543	4.41×10^{-8}	1.77×10^{-7}
^{173}Yb									19.4	0.569	4.01×10^{-8}	1.61×10^{-7}
^{175}Lu									32.9	0.671	3.16×10^{-8}	2.11×10^{-7}

uncertainties after level 1 and level 2 key rates have been determined. Fig. 11 illustrates how the uncertainties are reduced for each key rate level considered. The correlation coefficients for the level 1 key rates (Lv1) are underlined in Tables 4–6. The 3α reaction rate and the ^{56}Ni(n, p)^{56}Co rate, excluded from the MC variations, should be considered as level 0 key rates in our scheme, having top priority.

It is not surprising that (n, p) rates appear as key rates. They determine the flow into the next isotonic chain and the time-scale for proceeding to heavier nuclei. However, also (p, γ)↔(γ, p) rates are listed in Tables 4–6. At first glance, this may appear surprising because a (p, γ)↔(γ, p) equilibrium is established in the νp-process and in such an equilibrium the abundances do not depend on the individual proton capture or (γ, p) rates. The (p, γ)↔(γ, p) rates

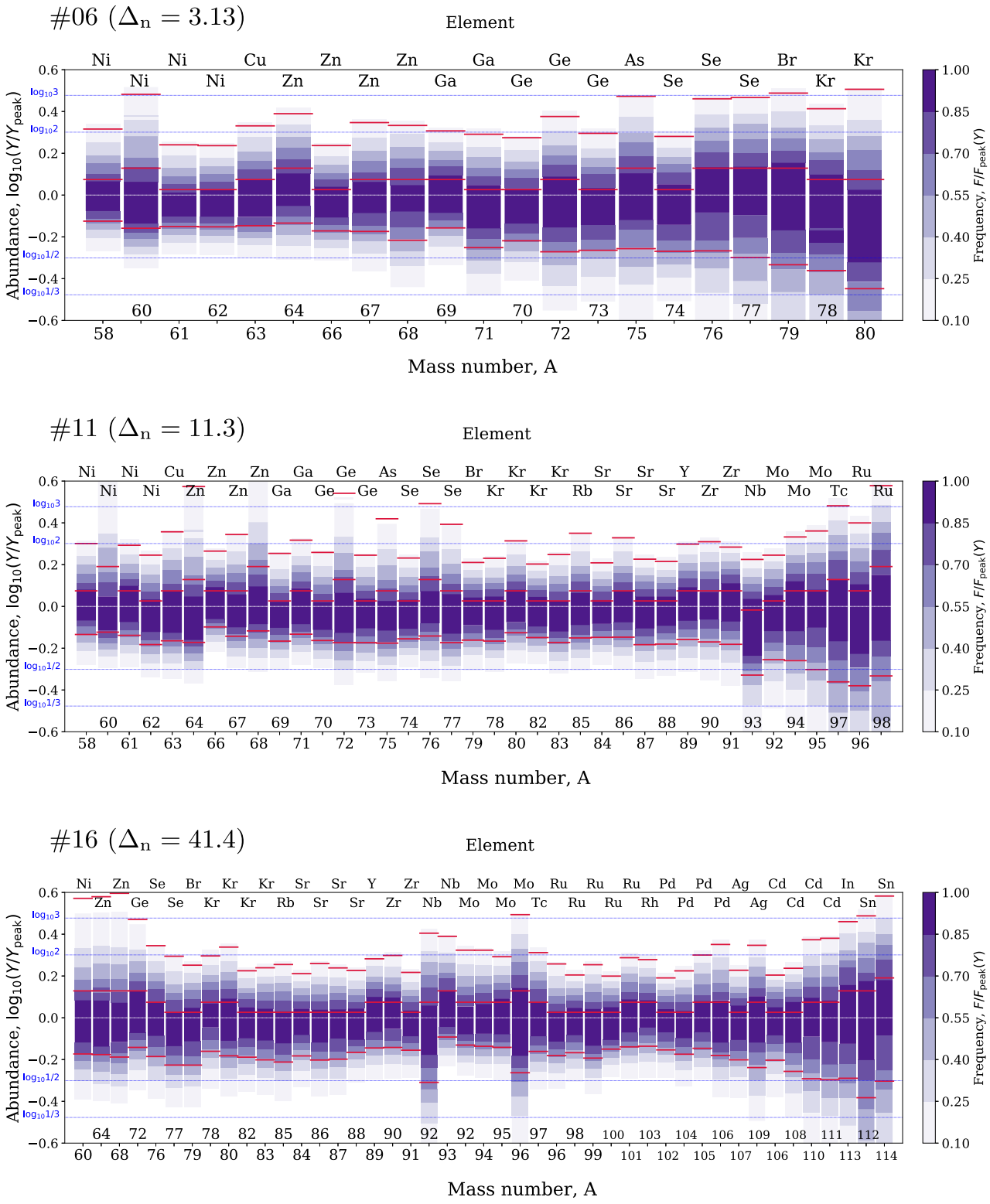

Figure 9. Total production uncertainties of stable nuclei due to rate uncertainties in the MC post-processing of the trajectories #06, #11, and #16. The colour shade gives the relative probabilistic frequency Y/Y_{peak} (final abundances Y normalized to the peak value Y_{peak}) and the horizontal red lines mark cumulative frequencies of 5 per cent, 50 per cent, and 95 per cent for each distribution. Uncertainty factors of 2 and 3 are marked by horizontal lines in blue. Note that the uncertainties are asymmetric and that the abundance scale is logarithmic.

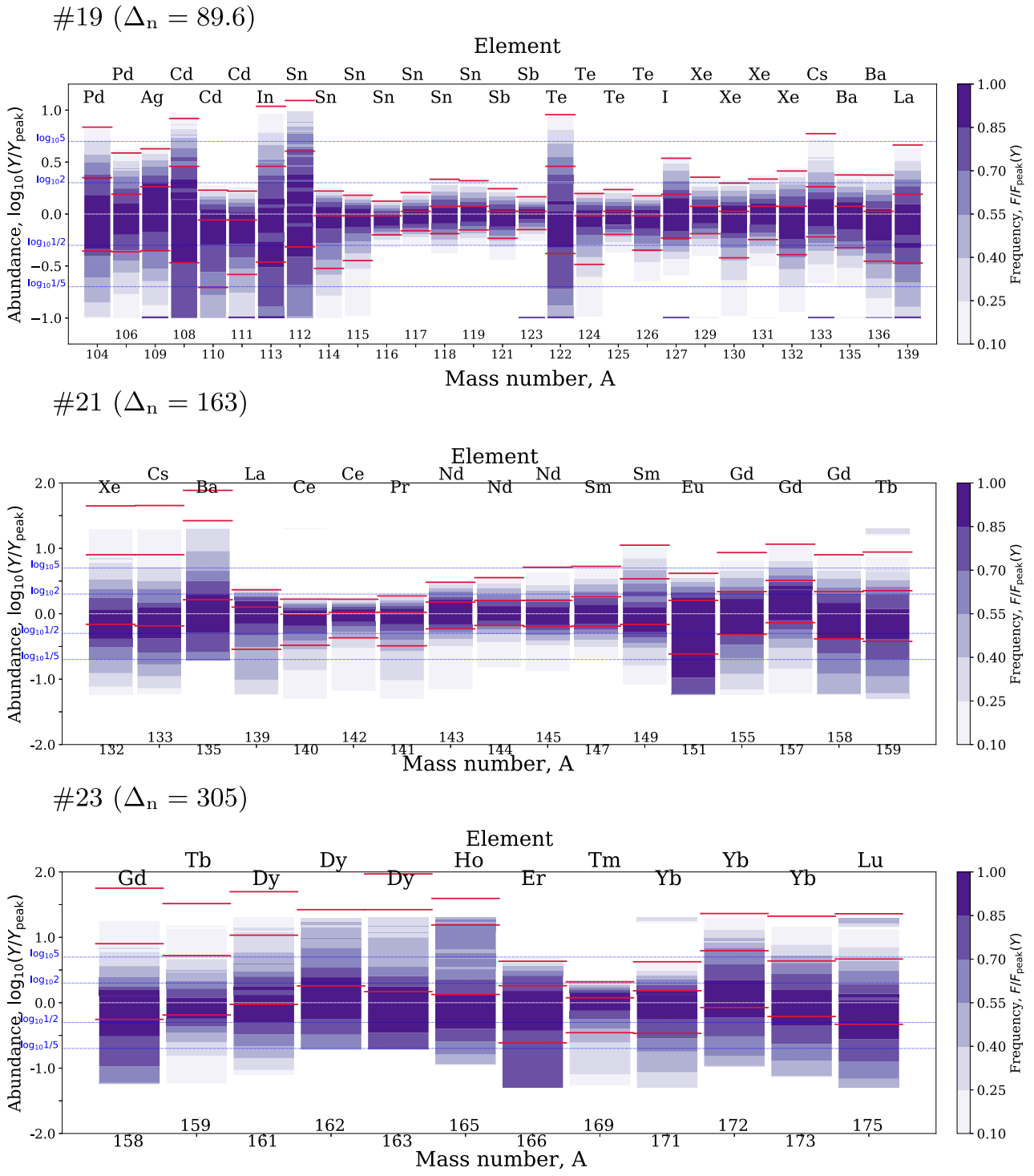

Figure 10. Same as Fig. 9 but for trajectories #19, #21, and #23.

found in the key rate tables, however, are at the edge of the reaction flows, where the rates are slow and either not equilibrated or fall out of equilibrium within our rate variations. Similar conclusions concerning the role of (n,p) reactions and proton captures were found by Fröhlich & Hatcher (2015), varying rates individually.

Neutron captures as key reactions are found in trajectories #15–#18. They are competing with (non-equilibrated) proton captures and push the reaction flow further towards stability and towards neutron-rich isotopes.

The impact of only varying (p,n)↔(n,p), (n,γ)↔(γ,n), or (p,γ)↔(γ,p) reactions, respectively, is shown in Fig. 12. This illustrates the effect of these reaction types in the different mass ranges. We emphasize, however, that only the MC variation of all reaction rates simultaneously provides a realistic assessment

Table 4. Key rates dominating the uncertainties for stable nuclides after decay of progenitors made in the νp-process for trajectories #01–#06 and their correlation coefficients r_{cor}. The correlation factors for the level 1 key rate (Lv1) are underlined.

Nucleus	Reaction	#01	#02	#03	#04	#05	#06
^{56}Fe	^{57}Co + p↔n + ^{57}Ni					0.67 (Lv3)	
^{56}Fe	^{56}Ni + α↔p + ^{59}Cu				0.78 (Lv3)		
^{57}Fe	^{56}Ni + p↔γ + ^{57}Cu	0.65 (Lv3)					
^{57}Fe	^{57}Ni + p↔γ + ^{58}Cu	−0.67 (Lv3)	−0.65 (Lv1)	−0.75 (Lv2)	−0.74 (Lv2)	−0.73 (Lv2)	−0.65 (Lv1)
^{59}Co	^{59}Zn(β$^+$)^{59}Cu	−0.94 (Lv3)			−0.92 (Lv3)	−0.90 (Lv3)	−0.88 (Lv3)
^{59}Co	^{59}Cu + p↔γ + ^{60}Zn				−0.70 (Lv2)	−0.73 (Lv2)	−0.75 (Lv2)
^{59}Co	^{59}Cu + p↔n + ^{59}Zn				−0.67 (Lv1)	−0.67 (Lv1)	−0.68 (Lv1)
^{58}Ni	^{58}Zn(β$^+$)^{58}Cu	−0.72 (Lv3)	−0.69 (Lv3)				
^{58}Ni	^{57}Cu + p↔γ + ^{58}Zn	0.69 (Lv2)	0.69 (Lv2)				
^{58}Ni	^{58}Cu + p↔γ + ^{59}Zn	−0.67 (Lv1)	−0.75 (Lv1)	−0.79 (Lv1)	−0.78 (Lv1)	−0.77 (Lv1)	−0.77 (Lv1)
^{60}Ni	^{59}Cu + p↔γ + ^{60}Zn	0.67 (Lv2)					
^{60}Ni	^{57}Co + p↔n + ^{57}Ni		−0.65 (Lv3)	−0.68 (Lv2)	−0.66 (Lv2)	−0.70 (Lv3)	
^{60}Ni	^{56}Ni + α↔p + ^{59}Cu				−0.66 (Lv3)		
^{60}Ni	^{60}Cu + p↔n + ^{60}Zn		−0.74 (Lv1)	−0.83 (Lv1)	−0.87 (Lv1)	−0.88 (Lv1)	−0.88 (Lv1)
^{61}Ni	^{60}Cu + p↔γ + ^{61}Zn	0.78 (Lv3)	0.75 (Lv2)	0.72 (Lv2)	0.69 (Lv2)	0.68 (Lv2)	0.66 (Lv2)
^{61}Ni	^{60}Zn + p↔γ + ^{61}Ga	0.67 (Lv2)					
^{61}Ni	^{61}Zn + p↔γ + ^{62}Ga	−0.65 (Lv1)	−0.74 (Lv1)	−0.78 (Lv1)	−0.77 (Lv1)	−0.77 (Lv1)	−0.77 (Lv1)
^{62}Ni	^{62}Zn + p↔γ + ^{63}Ga	−0.80 (Lv3)	−0.87 (Lv3)	−0.90 (Lv3)	−0.65 (Lv3)		−0.66 (Lv3)
^{62}Ni	^{62}Ga + p↔γ + ^{63}Ge	−0.71 (Lv2)	−0.69 (Lv2)	−0.65 (Lv2)	−0.66 (Lv3)		
^{63}Cu	^{63}Ge(β$^+$)^{63}Ga	−0.82 (Lv3)	−0.75 (Lv3)				
^{63}Cu	^{63}Ga + p↔γ + ^{64}Ge	−0.71 (Lv2)	−0.71 (Lv2)				
^{63}Cu	^{60}Cu + p↔n + ^{60}Zn	0.73 (Lv1)	0.67 (Lv1)				
^{64}Zn	^{60}Cu + p↔n + ^{60}Zn	0.90 (Lv1)	0.88 (Lv1)	0.69 (Lv1)			
^{64}Zn	^{64}Ga + p↔n + ^{64}Ge				−0.69 (Lv1)	−0.75 (Lv1)	−0.79 (Lv1)
^{67}Zn	^{67}As + p↔γ + ^{68}Se	−0.69 (Lv2)	−0.72 (Lv2)	−0.78 (Lv2)	−0.77 (Lv2)	−0.75 (Lv2)	−0.65 (Lv1)
^{68}Zn	^{64}Ga + p↔n + ^{64}Ge	0.77 (Lv1)	0.74 (Lv1)	0.73 (Lv1)			
^{68}Zn	^{68}As + p↔n + ^{68}Se				−0.78 (Lv2)	−0.83 (Lv2)	−0.70 (Lv1)
^{69}Ga	^{69}Se + p↔γ + ^{70}Br			−0.68 (Lv3)	−0.74 (Lv3)	−0.75 (Lv3)	−0.73 (Lv2)
^{69}Ga	^{68}As + p↔n + ^{68}Se	0.67 (Lv2)	0.65 (Lv3)	0.65 (Lv2)			
^{71}Ga	^{71}Br + p↔γ + ^{72}Kr				−0.70 (Lv3)	−0.71 (Lv3)	−0.73 (Lv2)
^{71}Ga	^{68}As + p↔n + ^{68}Se	0.66 (Lv2)					
^{70}Ge	^{70}Se + p↔γ + ^{71}Br					−0.65 (Lv3)	−0.68 (Lv2)
^{70}Ge	^{70}Br + p↔γ + ^{71}Kr						−0.71 (Lv3)
^{72}Ge	^{68}As + p↔n + ^{68}Se	0.77 (Lv2)					
^{72}Ge	^{72}Br + p↔n + ^{72}Kr					−0.69 (Lv3)	−0.77 (Lv2)
^{73}Ge	^{73}Kr + p↔γ + ^{74}Rb						−0.68 (Lv3)
^{75}As	^{72}Br + p↔n + ^{72}Kr	0.67 (Lv3)					
^{75}As	^{75}Rb + p↔n + ^{75}Sr						−0.67 (Lv3)

of the importance of a rate, as reflected in the definition of the key rates.

The reaction ^{59}Cu(p, α)^{56}Ni was identified as a level 3 (trajectories #04, #07–#09) or level 2 key rate (trajectories #10–#14) for the abundance of ^{56}Fe, the final decay product of ^{56}Ni after the νp-process has ceased, and for ^{60}Ni. This is part of a reaction cycle as described in Section 3.1. A stronger ^{59}Cu(p, α)^{56}Ni rate cycles material back to ^{56}Ni and hinders the flow to heavier masses (Arcones et al. 2012).

A few β$^+$ decays were identified as level 3 key rates: ^{58}Zn, ^{59}Zn, and ^{63}Ge. Their uncertainties would only become important after all other (n, p) reactions leading out of the respective isotonic chains have been determined.

An overview of all key reactions and how many nuclide abundances are affected by them is given in Table 7. At the top of the list, which is sorted by the number of reactions with significant impact, are (n, p) reactions, as expected.

Trajectories #07 and higher may contribute to the production of p-nuclides (see Section 1). The p-nuclides are underlined in Tables 5 and 6. Level 1 key rates concerning p-isotopes were only found in trajectories #15–#17. For $^{92, 94}$Mo, the key reactions are the proton captures ^{92}Mo(p, γ)^{93}Tc and ^{94}Ru(p, γ)^{95}Rh, respectively, indicating that these captures are not in equilibrium under the given conditions. The proton capture on the stable ^{92}Mo was also identified as a key reaction in the γ-process (Rauscher et al. 2016). In the νp-process, it acts at late times, altering the final ^{92}Mo abundance. Regarding the other trajectories, some do not contribute appreciably to the p-nuclides and in those which do, the uncertainties of several reactions are combined without a single dominating uncertainty.

The reproduction of the solar ^{92}Mo/^{94}Mo abundance ratio of 1.6 (Lodders 2003) in the rp- and νp-processes has been found to be problematic in previous studies (see, e.g. Woosley et al. 2004; Fisker, Hoffman & Pruet 2009; Wanajo et al. 2011; Xing et al. 2018). The abundance ratios of possible progenitor nuclides of these Mo isotopes within an isotonic chain are given mainly by the proton separation energies and therefore the attention in previous studies was focused on accurate mass determinations to tackle this problem. Masses are not varied in this MC study. We find, nevertheless, that uncertainties in the reaction rates affect not

Table 5. Same as Table 4 but for trajectories #07–#12. Underlined nuclides are p-nuclides.

Nucleus	Reaction	#07	#08	#09	#10	#11	#12
^{56}Fe	^{59}Cu + p↔γ + ^{60}Zn						− 0.65 (Lv3)
^{56}Fe	^{56}Ni + α↔p + ^{59}Cu	0.66 (Lv3)	0.69 (Lv3)	0.66 (Lv3)	0.66 (Lv2)	0.67 (Lv2)	0.68 (Lv2)
^{57}Fe	^{57}Ni + p↔γ + ^{58}Cu	− 0.66 (Lv1)	− 0.65 (Lv1)	− 0.66 (Lv2)	− 0.70 (Lv3)	− 0.70 (Lv3)	− 0.69 (Lv3)
^{59}Co	^{59}Zn(β$^+$)^{59}Cu	− 0.83 (Lv3)	− 0.76 (Lv3)				
^{59}Co	^{59}Cu + p↔γ + ^{60}Zn	− 0.77 (Lv2)	− 0.77 (Lv2)	− 0.78 (Lv3)	− 0.81 (Lv3)	− 0.81 (Lv3)	− 0.80 (Lv3)
^{59}Co	^{59}Cu + p↔n + ^{59}Zn	− 0.67 (Lv1)	− 0.66 (Lv1)	− 0.66 (Lv2)			
^{58}Ni	^{58}Cu + p↔γ + ^{59}Zn	− 0.75 (Lv1)	− 0.74 (Lv1)	− 0.71 (Lv1)	− 0.68 (Lv1)	− 0.70 (Lv3)	− 0.66 (Lv3)
^{60}Ni	^{59}Cu + p↔n + ^{59}Zn			− 0.75 (Lv2)	− 0.78 (Lv2)	− 0.74 (Lv2)	− 0.68 (Lv2)
^{60}Ni	^{60}Cu + p↔n + ^{60}Zn	− 0.88 (Lv1)	− 0.88 (Lv1)	− 0.87 (Lv1)	− 0.86 (Lv1)	− 0.85 (Lv1)	− 0.84 (Lv1)
^{61}Ni	^{60}Cu + p↔γ + ^{61}Zn	0.66 (Lv2)	0.66 (Lv2)				
^{61}Ni	^{61}Zn + p↔γ + ^{62}Ga	− 0.75 (Lv1)	− 0.72 (Lv1)	− 0.69 (Lv1)	− 0.71 (Lv2)	− 0.67 (Lv2)	− 0.65 (Lv2)
^{62}Ni	^{62}Zn + p↔γ + ^{63}Ga	− 0.67 (Lv2)	− 0.68 (Lv2)	− 0.69 (Lv3)	− 0.70 (Lv3)	− 0.70 (Lv3)	− 0.69 (Lv3)
^{62}Ni	^{62}Ga + p↔γ + ^{63}Ge	− 0.81 (Lv3)	− 0.80 (Lv3)				
^{63}Cu	^{63}Ga + p↔γ + ^{64}Ge			− 0.77 (Lv3)	− 0.74 (Lv2)	− 0.77 (Lv3)	− 0.75 (Lv3)
^{63}Cu	^{63}Ga + p↔n + ^{63}Ge		− 0.65 (Lv3)	− 0.67 (Lv2)	− 0.65 (Lv1)	− 0.67 (Lv2)	− 0.65 (Lv2)
^{64}Zn	^{63}Ga + p↔n + ^{63}Ge						− 0.65 (Lv2)
^{64}Zn	^{64}Ga + p↔n + ^{64}Ge	− 0.82 (Lv1)	− 0.84 (Lv1)	− 0.86 (Lv1)	− 0.86 (Lv1)	− 0.85 (Lv1)	− 0.85 (Lv1)
^{67}Zn	^{67}As + p↔γ + ^{68}Se	− 0.66 (Lv1)	− 0.66 (Lv1)	− 0.67 (Lv1)	− 0.67 (Lv1)	− 0.66 (Lv1)	− 0.67 (Lv3)
^{68}Zn	^{68}As + p↔n + ^{68}Se	− 0.76 (Lv1)	− 0.80 (Lv1)	− 0.82 (Lv1)	− 0.84 (Lv1)	− 0.85 (Lv1)	− 0.84 (Lv1)
^{69}Ga	^{69}Se + p↔γ + ^{70}Br	− 0.71 (Lv2)	− 0.68 (Lv2)				
^{71}Ga	^{71}Br + p↔γ + ^{72}Kr	− 0.72 (Lv2)	− 0.68 (Lv2)	− 0.67 (Lv2)	− 0.67 (Lv3)		
^{70}Ge	^{70}Se + p↔γ + ^{71}Br	− 0.69 (Lv2)	− 0.69 (Lv2)	− 0.65 (Lv1)	− 0.66 (Lv1)	− 0.68 (Lv1)	− 0.70 (Lv1)
^{70}Ge	^{70}Br + p↔γ + ^{71}Kr	− 0.71 (Lv3)	− 0.67 (Lv3)				
^{72}Ge	^{72}Br + p↔n + ^{72}Kr	− 0.66 (Lv1)	− 0.73 (Lv1)	− 0.77 (Lv1)	− 0.78 (Lv1)	− 0.79 (Lv1)	− 0.79 (Lv1)
^{73}Ge	^{73}Kr + p↔γ + ^{74}Rb	− 0.68 (Lv2)	− 0.69 (Lv2)	− 0.65 (Lv2)	− 0.65 (Lv3)		
^{75}As	^{75}Rb + p↔n + ^{75}Sr	− 0.72 (Lv2)	− 0.75 (Lv2)	− 0.67 (Lv1)	− 0.68 (Lv1)	− 0.67 (Lv1)	− 0.65 (Lv1)
^{74}Se	^{74}Kr + p↔γ + ^{75}Rb	− 0.67 (Lv2)	− 0.70 (Lv2)	− 0.70 (Lv2)	− 0.70 (Lv2)	− 0.66 (Lv2)	− 0.67 (Lv3)
^{76}Se	^{76}Rb + p↔n + ^{76}Sr	− 0.72 (Lv2)	− 0.67 (Lv1)	− 0.72 (Lv1)	− 0.74 (Lv1)	− 0.73 (Lv1)	− 0.71 (Lv1)
^{77}Se	^{77}Rb + p↔n + ^{77}Sr	− 0.69 (Lv3)	− 0.75 (Lv2)	− 0.72 (Lv1)	− 0.75 (Lv1)	− 0.74 (Lv1)	− 0.71 (Lv1)
^{78}Kr	^{78}Sr + p↔γ + ^{79}Y			− 0.66 (Lv3)	− 0.65 (Lv2)		
^{80}Kr	^{80}Y + p↔n + ^{80}Zr				− 0.66 (Lv3)		
^{85}Rb	^{85}Nb + p↔n + ^{85}Mo				− 0.65 (Lv3)	− 0.67 (Lv2)	− 0.65 (Lv3)
^{86}Sr	^{86}Nb + p↔n + ^{86}Mo					− 0.66 (Lv3)	

Table 6. Same as Table 4 but for trajectories #13–#18. Underlined nuclides are p-nuclides.

Nucleus	Reaction	#13	#14	#15	#16	#17	#18
^{56}Fe	^{59}Cu + p↔γ + ^{60}Zn	− 0.65 (Lv3)					
^{56}Fe	^{56}Ni + α↔p + ^{59}Cu	0.67 (Lv2)	0.65 (Lv2)				
^{57}Fe	^{57}Ni + p↔γ + ^{58}Cu	− 0.66 (Lv3)					
^{60}Ni	^{59}Cu + p↔n + ^{59}Zn	− 0.66 (Lv3)					
^{60}Ni	^{60}Cu + p↔n + ^{60}Zn	− 0.82 (Lv1)	− 0.81 (Lv1)	− 0.78 (Lv1)	− 0.75 (Lv1)	− 0.69 (Lv1)	
^{64}Zn	^{64}Ga + p↔n + ^{64}Ge	− 0.83 (Lv1)	− 0.80 (Lv1)	− 0.75 (Lv1)	− 0.70 (Lv1)		
^{68}Zn	^{68}As + p↔n + ^{68}Se	− 0.84 (Lv1)	− 0.81 (Lv1)	− 0.75 (Lv1)	− 0.68 (Lv1)		
^{70}Ge	^{70}Se + p↔γ + ^{71}Br	− 0.70 (Lv1)	− 0.68 (Lv1)	− 0.65 (Lv2)			
^{72}Ge	^{72}Br + p↔n + ^{72}Kr	− 0.78 (Lv1)	− 0.75 (Lv1)	− 0.66 (Lv1)			
^{76}Se	^{76}Rb + p↔n + ^{76}Sr	− 0.68 (Lv1)					
^{77}Se	^{77}Rb + p↔n + ^{77}Sr	− 0.69 (Lv1)	− 0.65 (Lv1)				
^{80}Kr	^{80}Sr + n↔γ + ^{81}Sr			− 0.65 (Lv2)			
^{93}Nb	^{93}Tc + n↔γ + ^{94}Tc				− 0.67 (Lv2)		
^{93}Nb	^{93}Tc + p↔γ + ^{94}Ru				− 0.70 (Lv3)		
^{92}Mo	^{92}Mo + p↔γ + ^{93}Tc				− 0.73 (Lv1)	− 0.71 (Lv1)	
^{94}Mo	^{94}Ru + p↔γ + ^{95}Rh		− 0.65 (Lv2)	− 0.65 (Lv3)	− 0.66 (Lv1)		
^{97}Tc	^{97}Rh + n↔γ + ^{98}Rh			− 0.70 (Lv1)	− 0.66 (Lv1)		
^{99}Ru	^{99}Rh + n↔γ + ^{100}Rh				− 0.65 (Lv3)		
^{100}Ru	^{100}Pd + n↔γ + ^{101}Pd				− 0.66 (Lv2)	− 0.68 (Lv1)	
^{113}In	^{113}In + n↔γ + ^{114}In					− 0.67 (Lv1)	
^{117}Sn	^{117}In + n↔γ + ^{118}In						− 0.74 (Lv1)

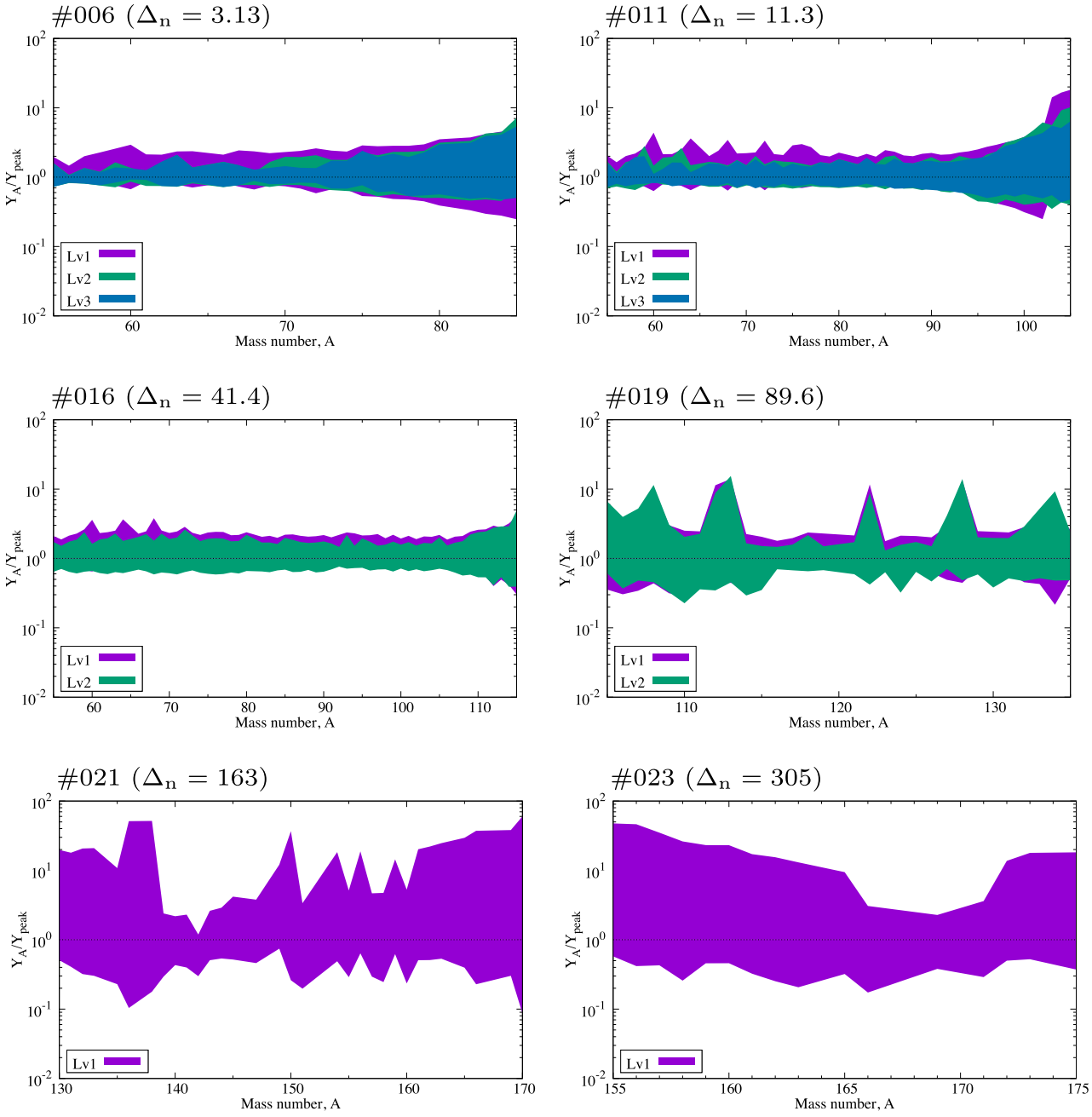

Figure 11. Final uncertainties obtained in six selected trajectories for several levels.

only the individual abundances of ^{92}Mo and ^{94}Mo but also their production ratio. This is because a leakage from an equilibrated (p,γ)↔(γ,p) chain can occur depending on the values of proton capture and (n,p) rates. Another reason is that the (p,γ)↔(γ,p) equilibrium is not fully upheld in trajectories only barely producing Mo.

Table 8 shows the uncertainties in the ^{92}Mo/^{94}Mo abundance ratio for selected trajectories. Although the standard rates do not reproduce the solar ratio, it is located within the 90 per cent confidence intervals defined by the 'up' and 'down' factors in all trajectories. This indicates that it is feasible to reproduce the solar value by adjusting reaction rates without modifying nuclear masses. It should be noted, however, that the most probable abundance values Y_{peak} also show the well-known problem of having too much ^{94}Mo relative to ^{92}Mo. Among the trajectories discussed here, trajectory #16 most efficiently produces the mass range of the Mo isotopes (see also Fig. 8).

The rate ^{92}Mo + p↔γ + ^{93}Tc (see, Mayer et al. 2016, and references therein, for relevance to the γ-process), which has been identified as a key rate for ^{92}Mo production, is also a key rate affecting the ^{92}Mo/^{94}Mo ratio. The correlation coefficients are r_{cor} = −0.66, −0.67, −0.65, −0.70, −0.74, −0.72, −0.72, and −0.68 for trajectories #16, #17, #18, #19, #20, #21, #22, and #23, respectively. The negative correlation indicates that the proton capture direction is dominating. An increase in the proton capture rate reduces the ^{92}Mo abundance and produces ^{94}Mo through flows via ^{93}Tc. Continuing from ^{93}Tc, two paths to ^{94}Mo are possible, either ^{93}Tc(p, γ)^{94}Nb(n, p)^{94}Tc(n, p)^{94}Mo or ^{93}Tc(n, γ)^{94}Tc(n, p)^{94}Mo. The flow via ^{94}Nb

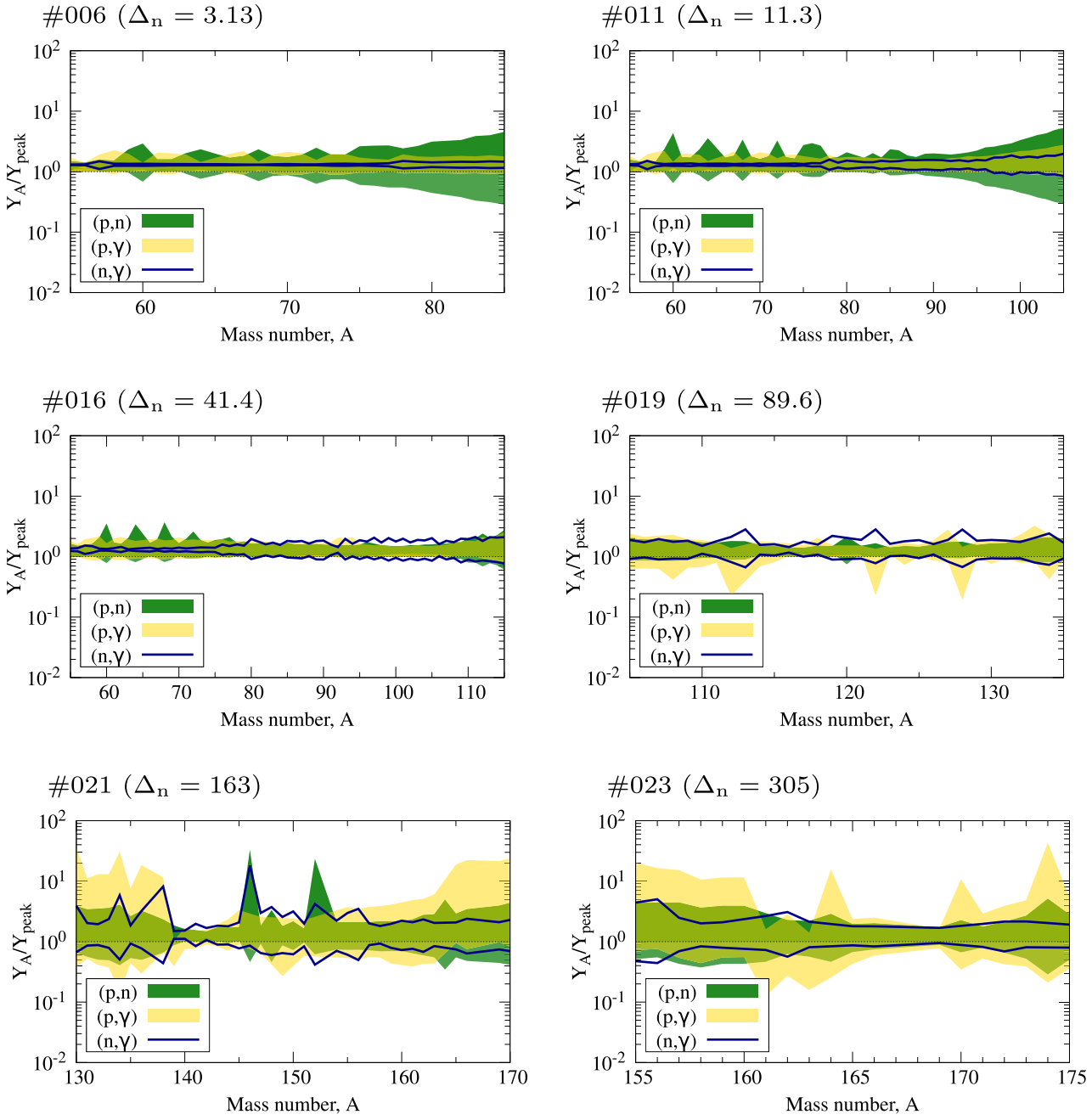

Figure 12. Final uncertainties obtained in six selected trajectories when only varying (p,n)↔(n,p), (n,γ)↔(γ,n), or (p,γ)↔(γ,p) reactions, respectively. Note that the mass number ranges are different in the different panels.

dominates in trajectories #11–#20. The participating reactions were not identified as level 1 key reactions, though. In addition, the (n, γ) and (p, γ) reactions on ^{94}Ru, followed by ^{93}Tc(p, γ)^{94}Ru, can also have a significant impact on the ^{92}Mo/^{94}Mo ratio by reducing the final ^{94}Mo abundance,[2] although they are not identified as key reactions.

Concerning the production of Kr, Sr, Y, and Zr (see Section 1), uncertainties of a factor of 2 are found for all stable isotopes of these elements, as seen in Table 2. As for the Mo isotope ratios discussed above, the reproduction of the solar abundances in the Kr–Zr region relative to the Mo region has proved difficult in previous studies of the νp-process (see, e.g. Wanajo et al. 2011; Xing et al. 2018). Table 8 also shows the abundances of ^{82}Sr and ^{78}Kr relative to ^{94}Mo. The solar value for the latter (0.82) is found, within uncertainties, in trajectories #19 and higher. The solar value of the ratio including ^{82}Sr (0.54), on the other hand, can only be reproduced (within uncertainties) at conditions around those represented by trajectory #19. Thus, conditions close to those of trajectory #19 can possibly simultaneously reproduce the abundance ratios of the Zr, Sr, and Mo isotopes. It has to be noted, however, that the

[2] ^{294}Mo is partially produced by ^{94}Ru after the νp-process via the decay series ^{94}Ru(β^+)^{94}Tc(β^+)^{94}Mo, of which half-lives are 3.11 × 10^3 s and 1.76 × 10^4 s, respectively.

Table 7. Key reaction list sorted by the number of affected nuclides per key rate level and by the counted number of involved trajectories.

Reaction	Level 1	Level 2	Level 3	Number of trajectories
^{60}Zn(n, p)^{60}Cu	^{60}Ni, ^{63}Cu, ^{64}Zn			17
^{64}Ge(n, p)^{64}Ga	^{64}Zn, ^{68}Zn			13
^{68}Se(n, p)^{68}As	^{68}Zn	^{68}Zn, ^{69}Ga, ^{71}Ga, ^{72}Ge	^{69}Ga	16
^{59}Zn(n, p)^{59}Cu	^{59}Co	^{60}Ni,^{59}Co	^{60}Ni	10
^{63}Ge(n, p)^{63}Ga	^{63}Cu	^{63}Cu, ^{64}Zn	^{63}Cu	5
^{72}Kr(n, p)^{72}Br	^{72}Ge	^{72}Ge	^{72}Ge, ^{75}As	12
^{57}Ni(p,γ)^{58}Cu	^{57}Fe	^{57}Fe	^{57}Fe	13
^{67}As(p,γ)^{68}Se	^{67}Zn	^{67}Zn	^{67}Zn	12
^{70}Se(p,γ)^{71}Br	^{70}Ge	^{70}Ge	^{70}Ge	11
^{77}Sr(n, p)^{77}Rb	^{77}Se	^{77}Se	^{77}Se	8
^{75}Sr(n, p)^{75}Rb	^{75}As	^{75}As	^{75}As	7
^{94}Ru(p,γ)^{95}Rh	^{94}Mo	^{94}Mo	^{94}Mo	3
^{61}Zn(p,γ)^{62}Ga	^{61}Ni	^{61}Ni		12
^{76}Sr(n, p)^{76}Rb	^{76}Se	^{76}Se		7
^{100}Pd(n,γ)^{101}Pd	^{100}Ru	^{100}Ru		2
^{58}Cu(p,γ)^{59}Zn	^{58}Ni		^{58}Ni	12
^{92}Mo(p,γ)^{93}Tc	^{92}Mo			2
^{97}Rh(n,γ)^{98}Rh	^{97}Tc			2
^{113}In(n,γ)^{114}In	^{113}In			1
^{117}In(n,γ)^{118}In	^{117}Sn			1
^{59}Cu(p,γ)^{60}Zn		^{59}Co,^{60}Ni	^{59}Co,^{56}Fe	11
^{59}Cu(p,α)^{56}Ni		^{56}Fe	^{56}Fe,^{60}Ni	9
^{57}Ni(n, p)^{57}Co		^{60}Ni	^{56}Fe,^{60}Ni	4
^{62}Zn(p,γ)^{63}Ga		^{62}Ni	^{62}Ni	12
^{60}Cu(p,γ)^{61}Zn		^{61}Ni	^{61}Ni	8
^{71}Br(p,γ)^{72}Kr		^{71}Ga	^{71}Ga	7
^{62}Ga(p,γ)^{63}Ge		^{62}Ni	^{62}Ni	6
^{63}Ga(p,γ)^{64}Ge		^{63}Cu	^{63}Cu	6
^{69}Se(p,γ)^{70}Br		^{69}Ga	^{69}Ga	6
^{74}Kr(p,γ)^{75}Rb		^{74}Se	^{74}Se	6
^{73}Kr(p,γ)^{74}Rb		^{73}Ge	^{73}Ge	5
^{85}Mo(n, p)^{85}Nb		^{85}Rb	^{85}Rb	3
^{78}Sr(p,γ)^{79}Y		^{78}Kr	^{78}Kr	2
^{57}Cu(p,γ)^{58}Zn		^{58}Ni		2
^{60}Zn(p,γ)^{61}Ga		^{61}Ni		1
^{80}Sr(n,γ)^{81}Sr		^{80}Kr		1
^{93}Tc(n,γ)^{94}Tc		^{93}Nb		1
^{93}Tc(p,γ)^{94}Ru		^{93}Nb		1
^{59}Zn(β^+)^{59}Cu			^{59}Co	6
^{70}Br(p,γ)^{71}Kr			^{70}Ge	3
^{58}Zn(β^+)^{58}Cu			^{58}Ni	2
^{63}Ge(β^+)^{63}Ga			^{63}Cu	2
^{56}Ni(p,γ)^{57}Cu			^{57}Fe	1
^{80}Zr(n, p)^{80}Y			^{80}Kr	1
^{86}Mo(n, p)^{86}Nb			^{86}Sr	1
^{99}Rh(n,γ)^{100}Rh			^{99}Ru	1

Table 8. Uncertainties of isotopic ratios in selected trajectories, given as uncertainty factors relative to the 50 per cent cumulative probability. The factors enclose a 90 per cent probability range. Also shown is the most probable value based on $Y_{\rm peak}$. The Solar system values are 1.6 for ^{92}Mo/^{94}Mo, 0.54 for ^{84}Sr/^{94}Mo, and 0.82 for ^{78}Kr/^{94}Mo (Lodders 2003).

	^{92}Mo/^{94}Mo				^{84}Sr/^{94}Mo				^{78}Kr/^{94}Mo			
Trajectory	$\frac{Y(92)}{Y(94)}\Big\|_{\rm peak}$	$\frac{Y(92)}{Y(94)}\Big\|_{50}$	Up	Down	$\frac{Y(84)}{Y(94)}\Big\|_{\rm peak}$	$\frac{Y(84)}{Y(94)}\Big\|_{50}$	Up	Down	$\frac{Y(78)}{Y(94)}\Big\|_{\rm peak}$	$\frac{Y(78)}{Y(94)}\Big\|_{50}$	Up	Down
#06	2.00	2.60	2.24	0.770	76.5	99.4	5.49	0.336	194	718	24.8	0.608
#11	0.923	1.20	2.14	0.793	1.86	2.41	3.03	0.627	2.18	2.83	3.64	0.547
#16	0.631	0.820	2.79	0.666	0.213	0.277	2.50	0.618	0.0837	0.109	2.76	0.573
#19	0.876	1.14	2.98	0.627	0.530	0.689	2.37	0.611	0.311	0.404	2.47	0.618
#21	0.980	1.27	2.87	0.675	0.664	0.862	2.25	0.744	0.390	0.507	2.32	0.733
#23	0.983	1.28	2.85	0.651	0.693	0.900	2.23	0.766	0.393	0.511	2.32	0.749

production of these nuclides is only marginal in this trajectory (see Fig. 8). The dominant production would be in the mass range $114 \lesssim A \lesssim 126$ and thus this region would be strongly overproduced relative to the lighter p-nuclides.

5 SUMMARY AND CONCLUSIONS

A comprehensive large-scale MC study of nucleosynthesis in the νp-process has been performed. A range of conditions in a Y_e and entropy parameter-space was explored to cover the possibilities regarding implementations of a νp-process in different sites. Our results allow to quantify the uncertainties stemming from nuclear physics input for any particular astrophysical simulation spanning this wide range of Y_e and entropy parameter-space.

For each of 23 chosen trajectories, and a choice for the 3α reaction and ^{56}Ni(n, p)^{56}Co reaction rates, the astrophysical reaction rates for several thousand target nuclides for Fe and above were simultaneously varied within individual temperature-dependent uncertainty ranges constructed from a combination of experimental and theoretical error bars. This allowed the investigation of the combined effect of rate uncertainties leading to total uncertainties in the final abundances of stable nuclei obtained after the νp-process had ceased. Key rates dominating the uncertainties in the final yields were determined. Different key rates were found for each trajectory, as the production range of nuclides depends on the thermodynamic conditions.

The rates for the 3α reaction and the ^{56}Ni(n, p)^{56}Co reaction were not included in the MC variation because their uncertainties dominate the production uncertainties of all nuclides and therefore would cover any other key rates. They should be considered as key reactions, nevertheless.

Among the other key reactions found, (n, p) reactions dominate because they determine the flow from one isotonic chain into the next. Most proton captures are in equilibrium and therefore their individual rates are not important. Several (p, γ) rates having been identified, as key rates are at the edge of the reaction flow or fall out of equilibrium within our variation limits. Among those is the proton capture on the stable nuclide ^{92}Mo, acting at late times and affecting the abundance of the p-nuclide ^{92}Mo, provided the conditions of trajectory #16 or #17 are found in nature. Similarly, the reaction ^{94}Ru(p,γ)^{95}Rh is a key reaction for the p-nucleus ^{94}Mo.

Concerning the isotope ratios of light p-nuclides it was found that it is possible to reproduce the solar ^{92}Mo/^{94}Mo abundance ratio within uncertainties, even though only rate uncertainties and not mass uncertainties have been considered. The reproduction of both the Mo isotopic ratio and their production level relative to the lighter p-isotopes of Kr and Sr has been found to be difficult within one trajectory. It has to be cautioned, however, that a contribution to the Mo isotopes stemming from the proton-rich side is severely constrained by the fact that live ^{92}Nb was found in the early Solar system, which cannot be produced by the decay of proton-rich unstable progenitor nuclei (Dauphas et al. 2003; Côté et al. 2019). It has to be noted further that realistic sites may give rise to a range of conditions, resembling a combination of several of our trajectories with different weights. The range of conditions and their respective weights may also depend on the specific nucleosynthesis site and may be different for different sites. A parameter study like this investigation is not devised to address such a superposition of conditions. Once site conditions have been constrained by hydrodynamic studies, however, our results can be used to assess the feasibility to reproduce abundance patterns of the Solar system and those found in meteorites. Therefore, for the time being – before having further constrained nucleosynthesis sites and reaction rates – it has to be concluded that a consistent production of the light p-nuclides (including the Mo isotopes) in the νp-process cannot be ruled out. We can also conclude that uncertainties in nuclear reaction rates may still have equal or even stronger impact than mass uncertainties on the path of the νp-process.

In summary, we found that the uncertainties in the production of nuclei are dominated by the uncertainties arising from the choice of site, explosion model, and numerical treatment of the explosion hydrodynamics, as these crucially determine what range of nuclei can actually be produced. Although the astrophysical constraints seem to be similarly weak for the νp-process as for the r-process, the νp-process is better constrained by nuclear physics and exhibits smaller uncertainties therein, at least in the dominating rates. Uncertainties stemming from the astrophysical reaction rates become important only after the nucleosynthesis conditions have been constrained better. Nevertheless, an experimental verification of the predicted rates will be difficult, not only because of the short-lived, intermediate, and heavy nuclei involved but also because of the high plasma temperatures, giving rise to considerable thermal excitation and thus small ground-state contributions to the stellar rate (Rauscher 2012, 2014). Importantly, even where feasible, experimental cross-section data typically only constrain these ground-state contributions. More promising is the experimental determination of nuclear properties required for the calculation of nuclear reaction rates. These include not only masses but, more importantly, also excitation energies, spins, and parities of excited states, both below the proton separation energy and in the relevant Gamow window. The determination of particle widths would improve constraints on the key reactions involving protons and α-particles. Present and future facilities using unstable beams offer possibilities for extracting such information.

ACKNOWLEDGEMENTS

The authors thank the reviewer for her/his valuable comments on the submitted manuscript. NN thanks T. Fischer for providing neutrino-driven wind trajectories used in this study. This work has been partially supported by the European Research Council (EU-FP7-ERC-2012-St Grant 306901, EU-FP7 Adv Grant GA321263-FISH), the EU COST Action CA16117 (ChETEC), the UK STFC (ST/M000958/1), and MEXT Japan ('Priority Issue on Post-K computer: Elucidation of the Fundamental Laws and Evolution of the Universe' and 'the World Premier International Research Centre Initiative: WPI Initiative'). GC acknowledges financial support from the EU Horizon2020 programme under the Marie Skłodowska-Curie grant 664931. CF acknowledges support by the U.S. Department of Energy, Office of Science, Office of Nuclear Physics, under Award No. DE-FG02-02ER41216. Parts of the computations were carried out on COSMOS (STFC DiRAC Facility) at DAMTP in University of Cambridge. This equipment was funded by BIS National E-infrastructure capital grant ST/J005673/1, STFC capital grant ST/H008586/1, and STFC DiRAC Operations grant ST/K00333X/1. DiRAC is part of the UK National E-Infrastructure. Further computations were carried out at CfCA, National Astronomical Observatory of Japan, and at YITP, Kyoto University. The University of Edinburgh is a charitable body, registered in Scotland, with Registration No. SC005336.

REFERENCES

Aikawa M., Arnould M., Goriely S., Jorissen A., Takahashi K., 2005, A&A, 441, 1195

Angulo C. et al., 1999, Nucl. Phys. A, 656, 3

Arcones A., Bliss J., 2014, J. Phys. G: Nucl. Phys., 41, 044005

Arcones A., Fröhlich C., Martínez-Pinedo G., 2012, ApJ, 750, 18

Bliss J., Witt M., Arcones A., Montes F., Pereira J., 2018a, ApJ, 855, 135

Bliss J., Arcones A., Qian Y.-Z., 2018b, ApJ, 866, 105

Caughlan G. R., Fowler W. A., 1988, At. Data Nucl. Data Tables, 40, 283

Cescutti G., Hirschi R., Nishimura N., Hartogh J. W. den ., Rauscher T., Murphy A. S. J., Cristallo S., 2018, MNRAS, 478, 4101

Cote B., Lugaro M., Reifarth R., Pignatari M., Vilagos B., Yague A., Gibson B. K., 2019, ApJ, 878, 156

Cyburt R. H. et al., 2010, ApJS, 189, 240

Dauphas N., Rauscher T., Marty B., Reisberg L., 2003, Nucl. Phys. A, 719, C287

Dillmann I., Heil M., Käppeler F., Plag R., Rauscher T., Thielemann F.-K., 2006, in Woehr A., Aprahamian A., eds, AIP Conf. Proc. Vol. 819, Capture Gamma-Ray Spectroscopy and Related Topics. Am. Inst. Phys., New York, p. 123

Fisker J. L., Hoffman R. D., Pruet J., 2009, ApJ, 690, L135

François P. et al., 2007, A&A, 476, 935

Freiburghaus C., Rauscher T., 1999, Reaction rate library in REACLIB format, available at: http://nucastro.org/reaclib.

Fröhlich C., Hatcher D., 2015, EPJ Web Conf., 93, 03008

Fröhlich C., Martínez-Pinedo G., Liebendörfer M., Thielemann F.-K., Bravo E., Hix W. R., Langanke K., Zinner N. T., 2006a, Phys. Rev. Lett., 96, 142502

Fröhlich C. et al., 2006b, ApJ, 637, 415

Fujibayashi S., Yoshida T., Sekiguchi Y., 2015, ApJ, 810, 115

Fynbo H. O. U. et al., 2005, Nature, 433, 136

Goriely S., 1999, A&A, 342, 881

Haettner E. et al., 2011, Phys. Rev. Lett., 106, 122501

Kizivat L.-T., Martínez-Pinedo G., Langanke K., Surman R., McLaughlin G. C., 2010, Phys. Rev. C, 81, 025802

Lodders K., 2003, ApJ, 591, 1220

Mayer J., Goriely S., Netterdon L., Péru S., Scholz P., Schwengner R., Zilges A., 2016, Phys. Rev. C, 93, 045809

Montes F. et al., 2007, ApJ, 671, 1685

Nishimura N. et al., 2012, ApJ, 758, 9

Nishimura N., Hirschi R., Rauscher T., St. J. Murphy A., Cescutti G., 2017, MNRAS, 469, 1752

Nishimura N., Rauscher T., Hirschi R., Murphy A. S. J., Cescutti G., Travaglio C., 2018, MNRAS, 474, 3133

Pearson K., Galton F., 1895, Proc. R. Soc. Lond., 58, 240

Pruet J., Hoffman R. D., Woosley S. E., Janka H.-T., Buras R., 2006, ApJ, 644, 1028

Rauscher T., 2012, ApJS, 201, 26

Rauscher T., 2014, AIP Adv., 4, 041012

Rauscher T., Thielemann F.-K., 2000, At. Data Nucl. Data Tables, 75, 1

Rauscher T., Dauphas N., Dillmann I., Fröhlich C., Fülöp Z., Gyürky G., 2013, Rep. Prog. Phys., 76, 066201

Rauscher T., Nishimura N., Hirschi R., Cescutti G., Murphy A. S. J., Heger A., 2016, MNRAS, 463, 4153

Rauscher T., Nishimura N., Cescutti G., Hirschi R., Murphy A. S. J., 2018, in Cheoun M., Hahn K. I., Jeong S., Kim S. C., Kwak K., Lee Y. S., Yoon S.-C., eds, AIP Conf. Proc., 1947, Origin of Matter and Evolution of Galaxies 2017, Am. Inst. Phys., New York, 020015

Sallaska A. L., Iliadis C., Champange A. E., Goriely S., Starrfield S., Timmes F. X., 2013, ApJS, 207, 18

Schatz H. et al., 1998, Phys. Rep., 294, 167

Takahashi K., Yokoi K., 1987, At. Data Nucl. Data Tables, 36, 375

Wanajo S., 2006, ApJ, 647, 1323

Wanajo S., Janka H.-T., Kubono S., 2011, ApJ, 729, 46

Weber C. et al., 2008, Phys. Rev. C, 78, 054310

Woosley S. E. et al., 2004, ApJS, 151, 75

Xing Y. M. et al., 2018, Phys. Lett. B, 781, 358

Xu Y., Takahashi K., Goriely S., Arnould M., Ohta M., Utsunomiya H., 2013, Nucl. Phys. A, 918, 61

This paper has been typeset from a TEX/LATEX file prepared by the author.